Tampere University

Oriol Pérez-De-Gregorio Busquets

NANOFABRICATION AND CHARACTERIZATION OF 3D PHOTONIC METAMATERIALS FROM VISIBLE TO THZ REGIME

ABSTRACT

In this work, I report on the fabrication and characterization of three-dimensional (3D) metamaterial structures with enhanced optical properties from visible (VIS) to terahertz (THz) spectrum regimes. The 3D metamaterials were fabricated by Direct Laser Writing (DLW) and coated utilizing Atomic Layer Deposition (ALD), using a compact custom build deposition system. Importantly, the fabricated 3D structures are mechanically and chemically stable. ALD depositions of zinc oxide (ZnO) are performed for each structure, showing a wide range of applications depending on unit cell size and geometry. Briefly, utilising nanoscale optical measurements I demonstrated periodicity-dependent optical resonances, enhanced sensitivity for refractive index detection of the surrounding medium, and asymmetric transmission for linearly polarised light. The proposed laser printing technique and conformal deposition recipes are ideal candidates for fabricating complex 3D metamaterial designs in a wide range of wavelengths leading to a collection of applications ranging from narrow-band filters and optical switches to direction selective absorbers and isolators. Hence, the study presented here may act as a guiding tool for integration of such 3D devices with technologies focusing on enhanced sensing, imaging, energy harvesting and telecommunications.[1,2]

Keywords: 3D metamaterials, direct laser writing, atomic layer deposition, refractive index, sensing, asymmetric transmission, nanophotonics, terahertz, infrared, split-cube resonator, woodpile.

PREFACE

This thesis work has been carried out in the Architectured Materials group at Empa Swiss Federal Laboratories for Materials Science and Technology, being a student enrolled in the Tampere University, as part of the Erasmus Mundus Joint Master Degree EURO-PHOTONICS.

A master's thesis cannot be completed without the help and support of other people. For all the scientific achievements reported, I would like to express my sincere gratitude and acknowledge, namely:

- Dr. Angelos Xomalis and Dr. Jakob Schwiedrzik for the guidance and mentoring over the course of this thesis. More specifically, Dr. Jakob Schwiedrzik for the scientific debates and Dr Angelos Xomalis for his knowledge, patience, for the hours that he devoted to read my drafts and thesis, and for all the great time spent together working side by side.

- Prof. Dr. Mircea Guina for his valuable help and advice through the thesis, and for accepting to be my examiner representing the Tampere University.

- All the people working at Empa (Thun) for their support, kindness, and for the good time spent, which made me feel part of their big family. Special mentions to Dr. Alex Groetsch, Jérémie Bérard, Léo Lapeyre, Dr. Elena Perivolari.

- My family, who unconditionally supported me in all the scientific steps and visited me wherever I went.

- All the people who supported and motivated me along this journey, with special mentions to Sergio Tovar, Berta Bosch, Alba Toro, Emma Portabella, and Lucero Cárdenas.

Tampere, 26 October 2022

Oriol Pérez-De-Gregorio Busquets

CONTENTS

LIST OF SYMBOLS AND ABBREVIATIONS

2D	Two-Dimensional
2PP	Two-Photon Polymerization
3D	Three-Dimensional
ALD	Atomic Layer Deposition
CMOS	Complementary Metal Oxide Semiconductor
CVD	Chemical Vapour Deposition
DiLL	Dip-In Liquid Lithography
DLW	Direct Laser Writing
EP	Electroless Plating
FCC	Face Centered Cubic
FEBID	Focused Electron Beam Induced Deposition
fs	Femtosecond
KF	Kelvin Foam
Mid-IR	Mid-Infrared
NIR	Near-Infrared
SCR	Split-Cube Resonator
SEM	Scanning Electronic Microscope
TEM	Transmission Electronic Microscope
THz	Terahertz
THz-TDS	Terahertz Time-Domain Spectroscopy
VIS	Visible
WD	Woodpile

1. INTRODUCTION

Since the beginning of humankind, the understanding and controlling of the material properties never ceased. In the past decades, this motivation has moved to nanoscience and nanotechnology, which allows us to study the thermal, mechanical, electrical and optical properties of materials at the atomic/molecule level, accomplishing extraordinary properties and expanding the materials discovery.[3] Recently, artificial structured materials, termed metamaterials, due to their unnatural features, emerged as promising materials offering an opportunity to further improve the capability of scientists to create material properties on demand. Diverging from the prior mentioned examples, the properties of metamaterials are not bounded to the intrinsic properties of the chemical constituents, but to the size and lattice constant of their constituent elements instead. These elements, commonly known as meta-atoms, function as atoms and molecules in traditional materials and allow efficient manipulation of electromagnetic waves; their optical properties can be spectrally tuned by varying the periodicity between meta-atoms, causing strong light-matter interactions over the entire electromagnetic spectrum.[4] Throughout the years, the research in metamaterials has been expanded and divided into different subareas depending on the mechanical, acoustic, electromagnetic properties. Here we focus on optical properties, one of the most promising with various applications in emerging technologies focusing on enhanced sensing, imaging, energy harvesting and photovoltaics.[3]
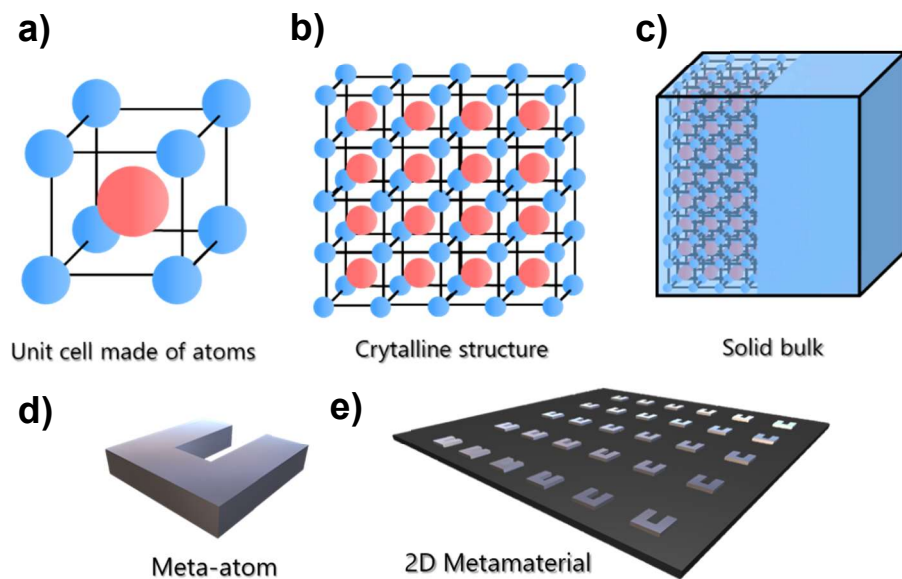
Figure 1. *Representation of conventional crystalline materials made of atoms creating unit cell (a) and a crystal (b and c). On the contrary, metamaterials made of meta-atoms (d and e).*

Additionally, there is a plethora of opportunities for fabricating three-dimensional (3D) metamaterials (see Figure 2), as they allow larger variety of structure designs, when compared to two-dimensional (2D) metamaterial designs. 3D volumetric structures comprise more subwavelength-scale resonators and offer more flexibility in the coupling between adjacent unit cells conforming the metamaterial. Fur-

Meta-atom

3D Metamaterial

Figure 2. *Representation of a mechanical (right) 3D metamaterial built up from meta-atoms (left).*

ther, 3D structures provide new properties like asymmetric transmission originated due to asymmetric coupling of magnetic resonances in the structure.[5] Till now, it is challenging to fabricate 3D metamaterials operating at optical wavelengths because of the sub-micron features of meta-atoms and their volumetric complexity. In the literature, it has been reported the fabrication of metallic woodpile structures operating at micron wavelengths using traditional lithographic techniques, but these can result in only a limited number of consecutive stacked layers, which are not trivial to align.[6,7] Moreover, one can utilize state-of-the-art lithography such as electron beam, where 10 nm resolution is achievable. However, it is a high-cost, slow and 2D limited fabrication process, essential qualities for practical applications. Thus, to date, the most used and successful method for the fabrication of 3D nanostructures is the Direct Laser Writing (DLW). This is a non-linear lithography technique based on two-photon polymerization (2PP) of photosensitive resins for the fabrications of 3D dielectric polymeric templates , resulting in cost-effective and high-resolution (~100 nm) fabrication. When a femtosecond (fs) pulsed laser is tightly focused inside the photoresist, the polymerization can be initiated by non-linear absorption within the focal volume of an otherwise transparent resist. Thus, high resolution features can be achieved when employing laser intensities that are above the non-linear polymerization threshold. Subsequently, the 3D geometries can be achieved by moving the laser focus through the photoresist using a 3D piezo stage or a galvo scanner. Hence, 3D metamaterials with a lateral resolution of about 100 nm can be fabricated.[8,9] It is worth mentioning that recent work has demonstrated a lateral resolution of almost 50 nm using stimulated-emission depletion DLW to fabricate woodpile structures.[10]
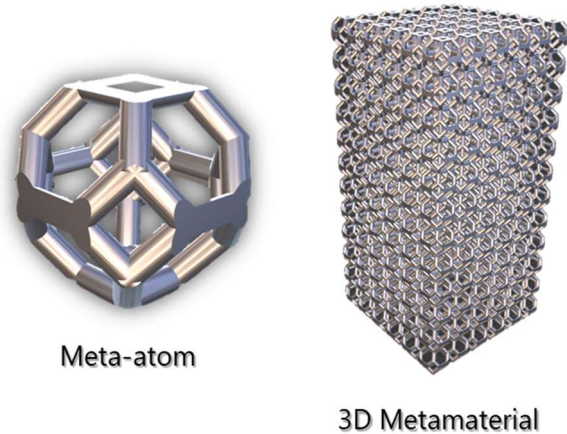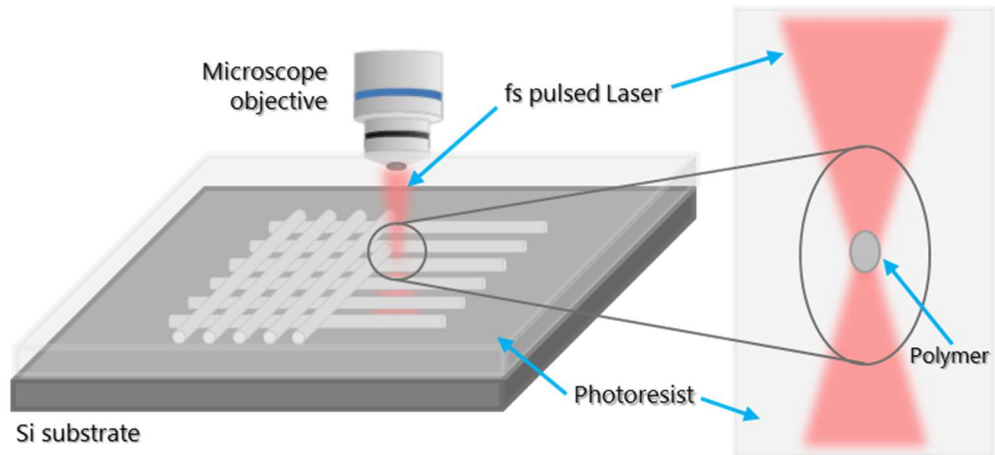
Figure 3. *Direct femtosecond (fs) Laser Writing technique. The laser beam is focused on a transparent resist resulting photopolymerization. By moving the beam or the stage one can achieve the fabrication of 3D high-resolution polymeric structures.*
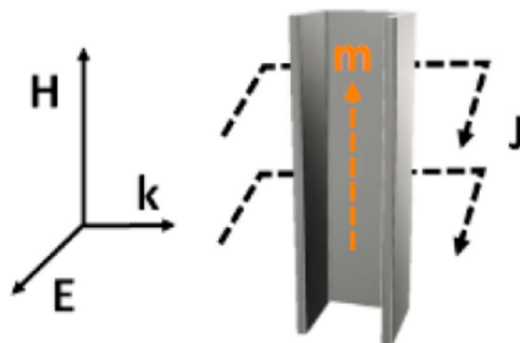
Furthermore, the metallization of these DLW structures is needed for the observation of their optical properties, since the photosensitive resins do not normally have a high refractive index and, therefore, the structures without any metallic or similar coating do not have a strong light-matter interaction. The resulting 3D polymer dielectric templates can be filled by electroplating if a positive photoresist (the part exposed to light becomes soluble to the photoresist developer) is employed. In the case of negative photoresists (the part exposed to light becomes insoluble to the photoresist developer), different techniques such as chemical vapor deposition (CVD), electroless plating (EP) and Atomic Layer Deposition (ALD) can accomplish a 3D metallization of the structures.[4,9,11,12] In ALD, the cycle-by-cycle thickness control and low defect density offers precise and reproducible depositions, as well as extreme surface conformality, uniformity, and a lack of porous. These ALD features are essential for the conformal coating of 3D structures at the nanometer scale, where other techniques, such as sputtering or evaporation can only achieve coating of flat surfaces.[12] Besides, ALD allows us to coat/deposit pure metals, oxides, nitrides, fluorides, sulfides, and II-VI and III-V compounds. For all these reasons this method is widely used in both industry and fundamental research.[13]

One material that is compatible with ALD processes is the well-known zinc oxide (ZnO). ZnO has attracted rapidly attention in the last years due to its potential in a vast number of applications including ultraviolet light emitters, piezoelectric transducers, photo-catalysis and -electrochemical cells for hydrogen generation, transparent electronics, and solar cells. Apart from its high thermal and chemical stability, ZnO comprise exceptional properties, such as a wide band gap in the range of ultraviolet wavelengths ($E_g \approx 3.37$ eV at room temperature), high electron mobility caused by its native n-type

doping due to oxygen vacancies or zinc interstitials, and biocompatibility.[14,15] Although, there are only few demonstrations in the literature about low-temperature ZnO films fabricated with ALD, and studies report mainly structural properties of ZnO thin films and different ALD recipes to improve these for certain applications, as well as combinations of other thin films, such as Al_2O_3, with the aim to find new mechanical features. Therefore, there is no existing research related to ALD deposition of ZnO in 3D metamaterials fabricated by DLW for the study of its optical properties, which can be undeniably interesting and give raise to new cost-effective applications.[16-18]

Lately, the scientific community focus on various geometries for meta-atoms, and consequently metamaterials. A broad range of geometries, depending on the desired optical properties, have been reported over the last decades.[19] More specifically, a geometry that has been around for some years in different research areas is the woodpile (WD) structure. As mentioned, previous studies have shown the realization of WD structures by using different fabrication methods, such as DLW. This structure has a relatively simple geometry that makes easier its fabrication and its periodicity induces optical bandgaps in a range of wavelengths that can be directly related to its size features. Additionally, this metamaterial has been reported as a 3D photonic-crystal emitter for thermal photovoltaic generation as well as a 3D plasmonic crystal for ultra-sensitive biosensing combined with a large surface for bio-immobilization, demonstrating its capabilities in a wide range of applications.[8-10]. Moreover, recent literature reported WD structures fabricated via DLW being photonic crystals acting as elementary building blocks that generate periodicity-dependent structural colours without any kind of coating.[20]

Another interesting geometry is the so-called Split-Cube Resonator (SCR). The nature of this meta-atom supports a strong magnetic resonance with an induced dipole moment when excited with a magnetic field parallel to its long axis (see Figure 4). This characteristic allows to create various structures with interesting optical properties just by designing metamaterials based on different arrangements of units of SCR.[4,21] It has already been reported the existence of asymmetric transmission as well as polarization-selective asymmetric perfect absorption for two metamaterials comprising the same meta-

Figure 4. Schematic of a SCR meta-atom interacting with an incoming electromagnetic wave. A magnetic dipole moment (orange) is induced when the light is polarised along the meta-atom's short axis. Extracted from Ref 21.

atom (SCR) but different unit cell.[4,5] However, these metamaterials based on SCR units are considering only metals as coatings limiting their applications.
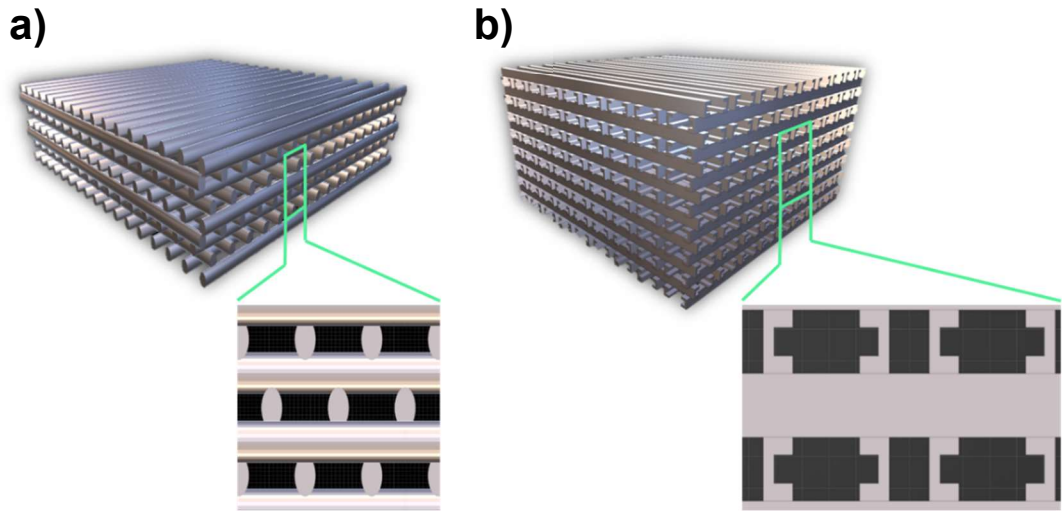
Figure 5. *3D representation of the metamaterials studied in this project. a) Woodpile (WD) and b) Split-Cube Resonator (SCR) structures. Insets show the unit-cell cross-section.*

In this thesis, I report the fabrication via DLW, the coating of ZnO made with ALD, and the optical characterization of 3D WD and SCR-based metamaterials. For the WDs, periodicity-dependent resonances were demonstrated with different coating thicknesses in the near-infrared regime (NIR). In the case of the SCR, asymmetric or angle-dependent transmission was demonstrated for uncoated and coated structures in the THz regime. In both cases, the ZnO enhances the electromagnetic properties of the metamaterials due to the increase of the effective refractive index. To my knowledge, this is the first report of 3D metamaterials coated with ZnO using ALD technique for enhanced electromagnetic resonances. Additionally, another SCR-based metamaterial is presented as a meta-device acting in the mid-infrared (mid-IR) regime. For this structure, I report the fabrication via DLW, the coating with selective electroless silver plating, and the characterization in the IR spectrum regime. This last metamaterial was part of a publication in the literature by Xomalis et al., and I had the honour to be one of the co-authors.[21] Thus, this study focuses on the methodology of the fabrication, coating (applicable to different 3D designs), and measurements of metamaterials in a wide range of wavelengths to act as guide for broad scope of applications in the nanophotonics field.

1.1   Physics of metamaterials

As briefly presented, metamaterials cover a wide range of areas thanks to its fascinating new properties such as the negative refraction, which attracted the scientific community interest in 2001.[22] Negative refraction is the phenomenon in which light rays are refracted in the opposite direction to which is normally expected from natural materials. Due to its exotic behaviour, this effect became one of the signature properties of the metamaterials physics and its demonstration offered a lot of new opportunities in the electromagnetic research, giving birth to the famous invisible cloak.[22] Thus, following this path, despite metamaterials present other interesting properties in areas such as mechanics (see Appendix), this work will be mainly focused on the electromagnetic properties of 3D metamaterials.

In order to understand how a metamaterial acts under the present of electromagnetic radiation is to study the behaviour of the meta-atoms, the basic unit that forms the metamaterial, as the physics behind are in many cases related to the resonant response of these. When an incident electromagnetic wave enters the metamaterial, oscillating electrical currents (J) are induced in the elements of each meta-atom, which are directly dependent to the geometric features of the meta-atoms (see Figure 6a). This response creates scattered secondary electromagnetic waves that form the macroscopic behaviour of the whole metamaterial, which we can classify as the well-known terms of reflection and transmission; the radiation scattered backward corresponds to reflection, and the one scattered forward corresponds to the transmission. Furthermore, this approach allows us to design structures where loops of conduction currents can be induced and, by Faraday induction, create magnetic dipole moments, proving artificial magnetism to otherwise not magnetic materials (see Figure 6b). In this kind of structures, the induced conduction currents are resonantly amplified, and the artificial magnetic response can be several orders of magnitude stronger than in materials found in nature.[22]

Based on this effect and following the comparison between atoms in conventional materials and meta-atoms in metamaterials, one could consider the meta-atom as a classical analogy of the atom, where the frequency of the resonance of the meta-atom would correspond to the energy of the atom's excited state and, by consequence, the electromagnetic waves scattered by the oscillating electrical currents would correspond to the emission of a photon when the atom transitions from an excited state to the ground state. Another way to understand the response of metamaterials would be to consider meta-atoms acting as antennas that for a specific design become resonators coupled to the

electric and magnetic fields of the incident wave at targeted wavelength, leading to strong electromagnetic scattering or dissipation as a result of amplified current oscillations.
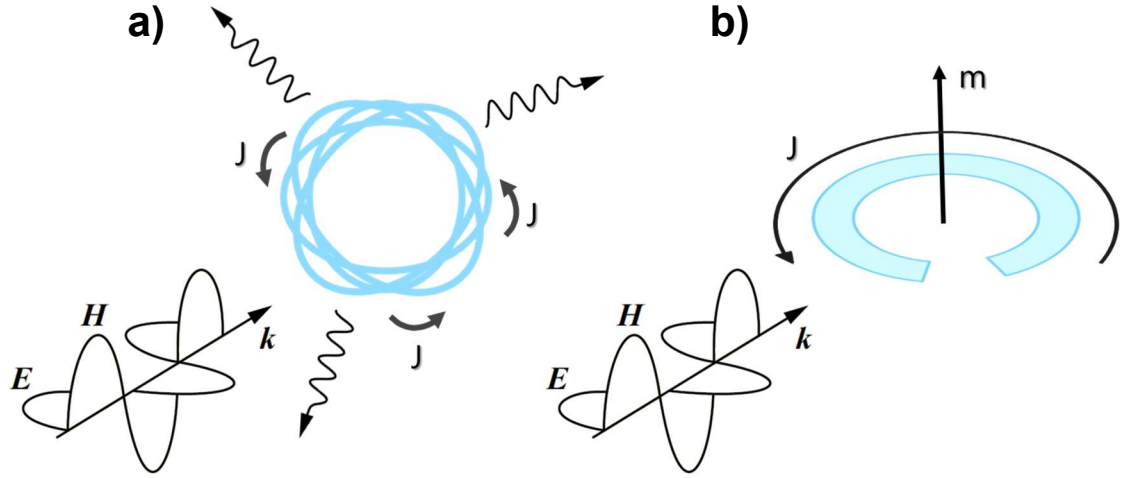
Figure 6. *Electromagnetic response of meta-atoms representing a) metallic wire resonators arranged randomly and b) a split wire ring showing a geometrical resonance upon light illumination, which induces a magnetic dipole moment m (artificial magnetism). Adapted from chapter 56.1 in Ref 22.*

Another important characteristic of metamaterials comes from the dependency of the oscillating electrical currents with the geometric features of the meta-atoms. By modifying the structural dimensions of the meta-atoms, we can tune at any wavelength the metamaterial resonances. Moreover, meta-atoms hold resonant modes analogue to the ones found in electromagnetic cavity resonators or mechanical vibrating string (Figure 6b acts as such), which is due to the excitation of standing waves of electrical currents along their structure. With these two concepts in mind, one can estimate the wavelengths of the supported resonances in the meta-atoms by using the following formula:

$$\lambda_o \approx \sqrt{\varepsilon}\ \frac{2l_e}{m} \tag{1}$$

where l_e is the total electrical (antenna) length of the pattern that forms the meta-atom, ε is the effective permittivity of the overall system, and m is a positive integer that represents the order of the resonance, which normally is limited to 4, as subwavelength meta-atoms can only support the first resonances, since $l_e > \lambda_o$.[22]

It is important to distinguish the photonic crystals and metamaterials, as it is directly related to the light-matter interaction and the dimensions of the structures. The main characteristic that defines photonic crystals is the photonic bandgap, which it can be achieved by tailoring the periodicity of their unit cell at the same or larger of the wavelength they interact with, because the effect of the bandgap arises from diffraction. On

the contrary, metamaterials, as it can be demonstrated in eq.1, have subwavelength features that they do not show diffraction. Another remarkable point to differentiate them is that photonic crystals are not homogeneous, so one cannot define values of permittivity or permeability, which are essential parameters when working with metamaterials, as the wavelength passing through a metamaterial has to "see" an effective medium (overall) response that is occurring only when the unit cell is deeply subwavelength.

Now, in order to have all these mentioned effects, one important requisite must be fulfilled: the material which the meta-atoms are made of must be good conductor in the electromagnetic range of the incident wave; that is the reason why metals are the main choice when working with optical metamaterials, as they support oscillating electrical charges (plasmons), analogue to the large-scale electrical current in circuits all the way down to the near-IR. Additionally, it is well-known that metals exhibit negative permittivity from the visible range allowing strong plasmonic resonances. Thus, in presence of an electromagnetic wave, metals show high light-matter interactions due to their refractive index, which is a key parameter when studying the electromagnetic response in metamaterials. Further, apart from plasmonic materials, strong resonances can be obtained utilising dielectric metamaterials where, instead of oscillating charges (plasmons), they utilize displacement volumetric currents.[22] In this thesis we will show, for the first time, that tuneable metamaterial resonances can be also obtained with ZnO coatings where the refractive index is expected to be smaller than 2.

2. METHODOLOGY

2.1 Direct Laser Writing

DLW is a technique that uses multi-photon polymerization with the aim to fabricate 3D assembled structures with a resolution down to 100 nm. In this section, the main working principle, the setup, the materials, and the software used in this project are described in detail.

2.1.1 Multiphoton absorption

The physical phenomenon behind the DLW is the multiphoton absorption; for simplicity, the two-photon absorption is the one described in this chapter.

Two-photon absorption, a third-order process with respect to the order of the nonlinear susceptibility, is defined as the absorption of two photons of identical or different energies that excite a molecule from one state (or energy level) to a higher one, being the sum of the absorbed photons equal to the energy difference of the states involved in the
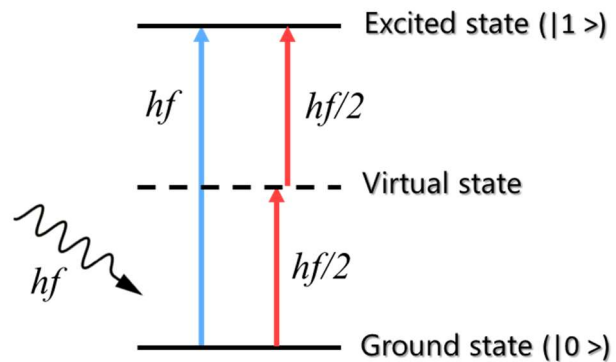
Figure 7. *Energy levels diagram and representation of energy transitions in single- (blue) and two-photon (red) absorptions.*

transition (see Figure 7). Even though it is a third-order nonlinear process, regarding to light intensity it is a second-order (proportional to the square of the local intensity) and, for this reason, when compared to the linear absorption (one photon gets absorbed and the transition is between two states with exactly the same energy difference as the photon has), the nonlinear process is several orders of magnitude weaker. In other words, in order to increase the number of such rare events, high light intensities are required, which are normally achieved with fs pulsed lasers. Furthermore, this is the reason why the two-photon absorption is employed, as the polymerization will only occur in small volumes where the intensity of the laser is high enough to surpass the polymerization threshold.[23] This small volume where the polymerization will occur is commonly known as voxel and, as we will see through this work, the size of it will depend on the laser focusing, laser power, and the type of photoresist employed.

2.1.2 Experimental setup and materials

Here we use a conventional nanoprinter (Nanoscribe Photonic Professional GT) for DLW. A schematic representation of the optical setup inside the device can be seen in the Figure 8.
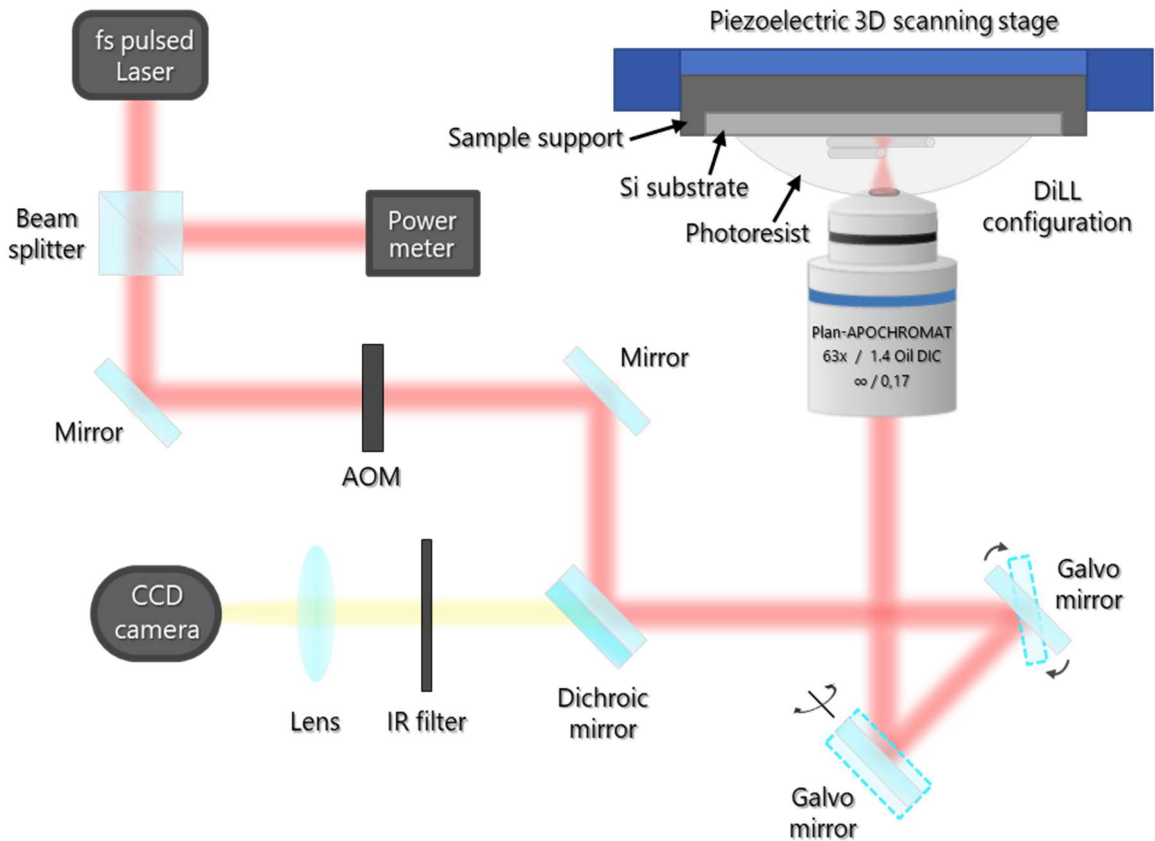
Figure 8. *Typical setup of a Direct Laser Writing (DLW) system in Dip-in-Laser Lithography (DiLL) style configuration, consisting of: light source (fs laser), beam and sample motion systems, focusing optics, and a CCD camera.*

As it can be observed, the system is based in components such as: fs laser, beam, and sample movement elements, focusing optics, and a vision system. In the case of the laser source, a Ti:Sapphire femtosecond laser is integrated. This laser is operating at a center wavelength of 780 nm, 25 kW peak power, 100 fs pulse duration, and 80 MHz repetition rate.[24]

The beam and sample motion systems consist of galvanometric scanners (move the beam focus) and a piezoelectric 3D scanning stage (moves the stage). In order to fabricate 3D structures, one has to choose between the two modules. On one hand, when using the galvanometric stages, a layer-by-layer or sliced structure is fabricated, and a moving stage is lifting the sample when a layer is completed. On the other hand, the piezoelectric stage does not require the slicing of the structure, as it can be moved

in all directions with extremely high accuracy of nanometers. The decision between these two motion modules depends on the desired times of fabrication, accuracy, and size of the structure. The galvo scanners have higher scanning speeds (100x faster than piezo) and larger working lengths, but the beam can be distorted as it moves due to the microscope objective, which does not provide a perfect flat field-of-view. The piezo stage is much slower and covers less range but, as mentioned, can provide much more accuracy (see Table 1 for working lengths of each scanner).[23-25]

Table 1. *Working lengths for the motion modules. Values subtracted from Ref 25.*

Objective	x-y dimension	z height
25x NA 0.8	> 200 µm (Galvo) > 300 µm (Piezo)	> No limit (z-drive) > 300 µm (Piezo)
63x NA 1.4	> 400 µm (Galvo) > 300 µm (Piezo)	> No limit (z-drive) > 300 µm (Piezo)

For the focusing optics, it is required a microscope objective to tightly focus the laser beam and achieve high intensities and high structuring resolution. In this system, we have a microscope objective facing the substrate and immersed into the liquid photoresist for an aberration-constant printing, which corresponds to a Dip-in-Laser Lithography (DiLL) configuration that enables a precise microfabrication even on opaque substrates. The advantage of DiLL configuration over the common immersion of oil objective is that allows to fabricate much higher 3D microstructures, as one of the main disadvantages of using microscope objectives is the short working distance and the immersion in oil requires the objective facing towards the other side where the structure is fabricated, and consequently, the substrate needs to be highly transparent to the wavelength of the laser.[23]

Thanks to the versatility of our printing system, there is the possibility to use different microscope objectives depending on the scale and desired resolution of the metamaterial designs. In this work, all the metamaterials were fabricated making use of 25x and 63x magnification microscope objectives (see Table 2 for more details). Additionally, two types of photoresists were applied depending on the microscope objective used: IP-S for the 25x objective and IP-Dip for the 63x objective. The 25x objective immersed in IP-S was chosen for mesoscale structures with high proximity effect and low shrinkage, while the 63x objective with IP-Dip was used to fabricate high resolution features as well

as for index matching with the high numerical aperture (NA) microscope objective (see more details in Table 2).

Table 2. *Microscope objectives used in DLW with its respective photoresists and typical voxel dimensions. Values subtracted from Ref 24.*

Objective	Immersion medium	Photoresist	x-y voxel diameter	z voxel height
25x NA 0.8	Resist (DiLL config.)	IP-S	< 600 nm	< 3000 nm
63x NA 1.4	Resist (DiLL config.)	IP-Dip	< 200 nm	< 700 nm

The typical photoresists are conventionally composed by a monomer, a photoinitiator, which absorbs the laser radiation and provides the active species that starts the polymerization. In order to ensure that the multiphoton absorption phenomenon takes place, these photoresists must fulfill some requirements such as: (I) both components of the photoresist need to be transparent to the wavelength of the laser employed, (II) the monomer needs to be transparent at the two-photon absorption wavelength, and (III) the photoinitiator needs to absorb the two-photon absorption wavelength and have high two-photon absorption cross-section, high radical quantum yield and highly-active radical species generated. In our case, the two photoresists were strictly chosen from the same industrial provider as the DLW equipment, thus, they fulfill every aspect.
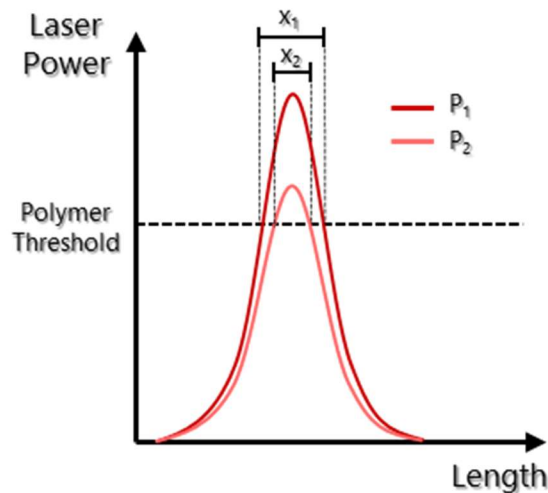
**Figure 9.** *Laser power dependency of the voxel size in DLW.*

Furthermore, the resolution of the fabrication depends on the laser power strongly. In order to achieve photopolymerization, a polymer threshold (given by the initiator absorption cross-section), which is the minimum laser power that is required to polymerize in the tightly focused area, has to be surpassed. Once this threshold is reached, as more

power is employed, the wider the voxel size becomes, because the area which has enough energy to be polymerized turns larger (see Figure 9 where $P_1 > P_2$). Thus, to accomplish the best resolution, one has to carry out a detailed study of laser power to search for this polymer threshold. However, as mentioned, there is a minimum voxel size that can be achieved depending on other parameters such as microscope objective magnification and photoresist. Another important factor to take into account is that the photoresist can be burned if the laser is focused in the same spot for a long period of time with a high laser power value or air bubbles created inside the photoresist. Both effects can complicate the fabrication to such an extent of not having the metamaterial at all.

Finally, it is important to mention the effect of utilizing a reflective substrate during the fabrication in DiLL configuration. As it was explained, DiLL configuration allows the use of any kind of substrate, even opaque, but when a highly reflective substrate (in the wavelength of the laser) is employed, an interference (standing wave) can be created close to the substrate. The beam focused in the first layers of the polymers interfere constructively and destructively with the beam reflected backwards from the substrate and the polymerization takes place in such interference pattern (see Figure 10). In our case, the Si substrate shows such an effect, however, it was only present in the first layers and did not affect the overall performance of the metamaterial.
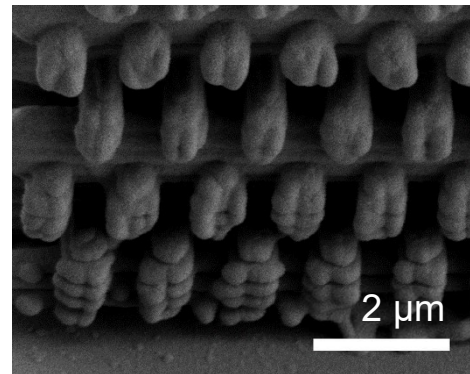
Figure 10. *SEM image of the WD structure. The interference pattern due to the highly reflective substrate (here Si) can be seen in the first row of piles and decreases with distance.*

2.1.3   Design software

Once the model for the desired structure is prepared, the Nanoscribe Photonic Professional GT using a software called DeScribe that converts the 3D structures in .stl format to the internal language of the laser writer. Here the 3D file turns into trajectories that the laser will expose to polymerize the photoresist. Thus, the description of the most important parameters in the DeScribe software and how they affect the fabrication are presented in this section.

First, when the .stl file is imported in the DeScribe, one chooses which objective, photoresist and substrate will be used during fabrication, as the program will take them into account due to their effect in the resolution. Then, three windows (see Figure 11) are opened: Slice, Fill and Output, in that order.

The Slice window is where the structure is divided into layers of a fixed distance in the z-plane (see Figure 12a and 12b for comparison of two different slice distances). The less distance is specified in it, the more divisions of the structure and the longer it takes to fabricate. The program does not set a limit of minimum distance and one can go as small as it can, but it is important to keep in mind that this is a simulation, and the software does not take into account the voxel size yet (or the minimum step of the stage).
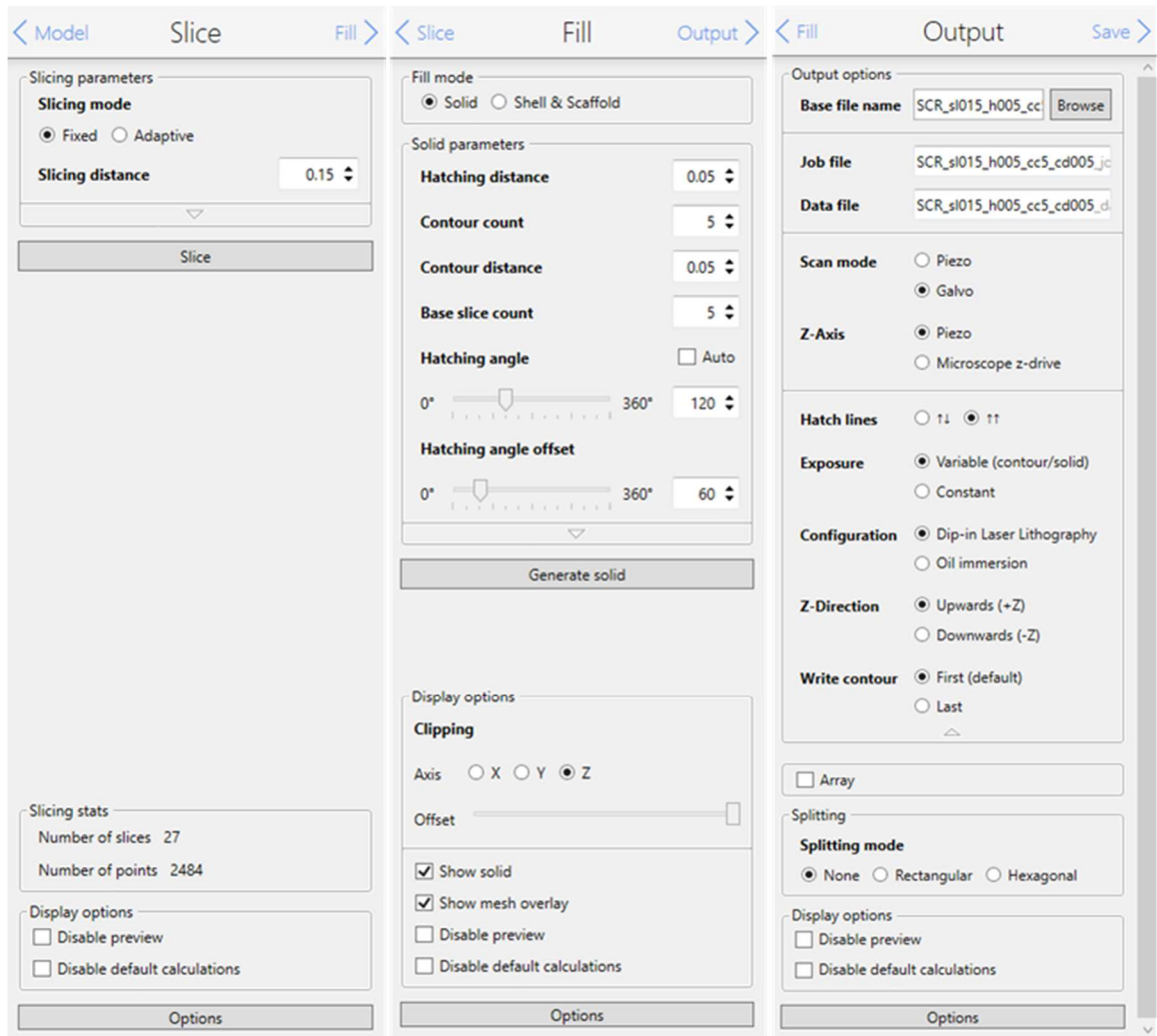
Figure 11. *The different steps in the DeScribe 2.6 program, where the 3D structure (.stl file format) is converted to the internal language format of the laser printer (Nanoscribe Photonic Professional GT).*

The second window, called Fill, shows more fabrication parameters. First one is the hatching distance, which is the analog of the slicing but laterally; divides the structure in x and y for each layer set in the previous step. Then, the contour count is described as the number of lines that follow the contour of the structures, and it is coupled to the contour distance, which appears at 2 or more contour count, as it is the distance between the lines in the contour of the structure. Next, the base slice count, a parameter that defines the number of layers close to the substrate written with the minimum hatching distance to ensure good binding of the structure to the substrate. Normally, this last parameter is set higher as the models are taller; the taller the structure, the more stability it needs in the base to maintain its shape and not collapse. Last but not least, the hatching angle and the hatching angle offset. Basically, these two parameters settle the angle between the laser and the structure, so that the hatching defined previously can be set parallel, perpendicular or with low angle, with respect to the structure. It can be observed in Figure 12c and 12d a comparison of two hatching distances, as well as two contour count values with two contour distances; the structure in 12d looks much robust and solid but it takes longer fabrication time and several voxels could probably be overlapped.[25]
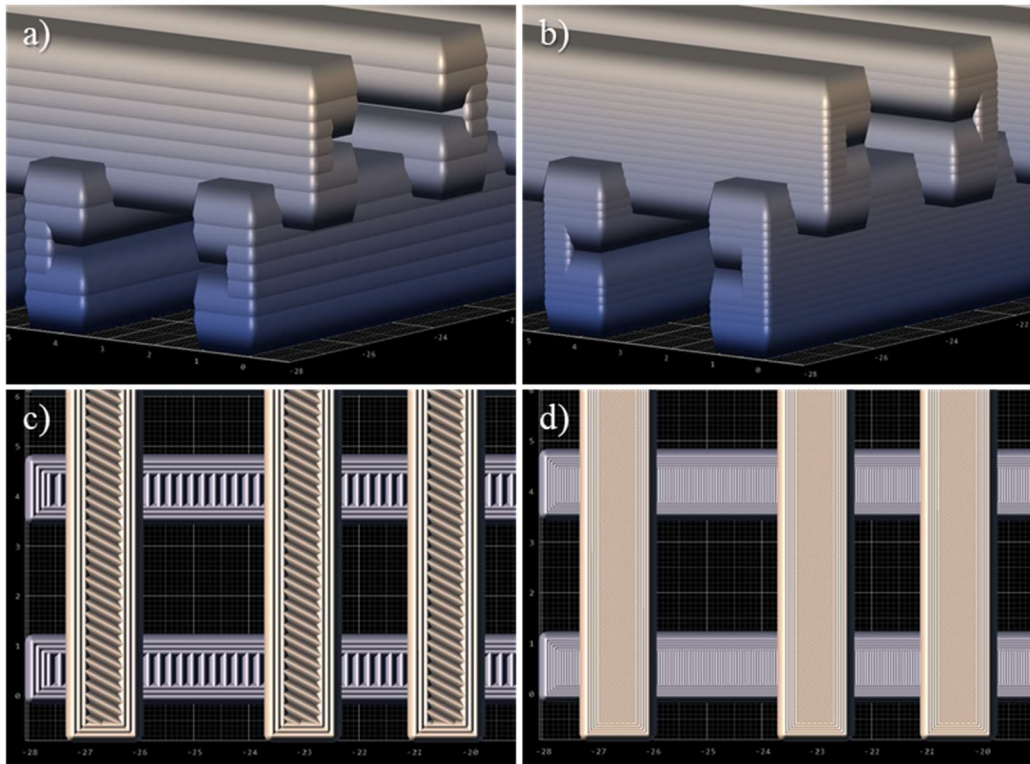

Figure 12. *Simulations of the effect of slicing (a and b) and hatching distance (c and d) in the SCR structure.*

Last window, the Output, is the previous part to saving the "job"; the file that the internal language of the laser printer will recognize. In this part, one can define the name of the file and where to save it, the scan modes in x and y and z, and other parameters related to the setup and modelling. The scan modes refer to the aforementioned galvanometric and piezoelectric scanners, while the other parameters refer to the configuration of oil immersion or DiLL, the z-direction during fabrication, among others. Additionally, when a structure is too large for any kind of scanners and microscope objectives (see Table 1), the splitting mode in this window divides the structure in different sections that will be completed one after the other by placing the moving stage of the printer along the different regions. This mode has integrated parameters that define how the different regions of the metamaterial should be attached. In short, this mode allows us to fabricate structures of several millimeters.

2.1.4 Preparation and development of samples

Reached this point, with the structure modeled and converted into a Nanoscribe laser writer compatible file, the next step is to prepare the substrate and start the fabrication in the cleanroom, where the laser printer is installed. It is mandatory to work in a cleanroom environment due to several contaminants such as gases and particles that can negatively affect product yield. In cleanroom, the resist and fabrication process are isolated from particles that could potentially damage the microstructures. Our cleanroom, in Empa building in Thun (Switzerland) is class 10.000 or ISO 7 and has yellow light filtration ideal for photosensitive materials, which is required from the photoresists employed.

First of all, a Si substrate of 1x1 cm^2 is cut from a Si wafer (wafer dicing). This Si substrate, previously prepared with a photoresist film so it does not get contaminated, is submerged in acetone (Microchemicals GmbH) for 30 seconds approximately, then washed with isopropanol (Microchemicals GmbH), and dried with a nitrogen gun. Once the substrate is dry, it is placed in one of the sample holders of the laser printer and attached with tape. Finally, a droplet of the photoresist (IP-S or IP-Dip) is placed on top of the substrate, ideally without any bubbles inside, and rested there until spreads over the surface (see Figure 13). Now, the sample is ready to be inserted in the Nanoscribe laser writer.
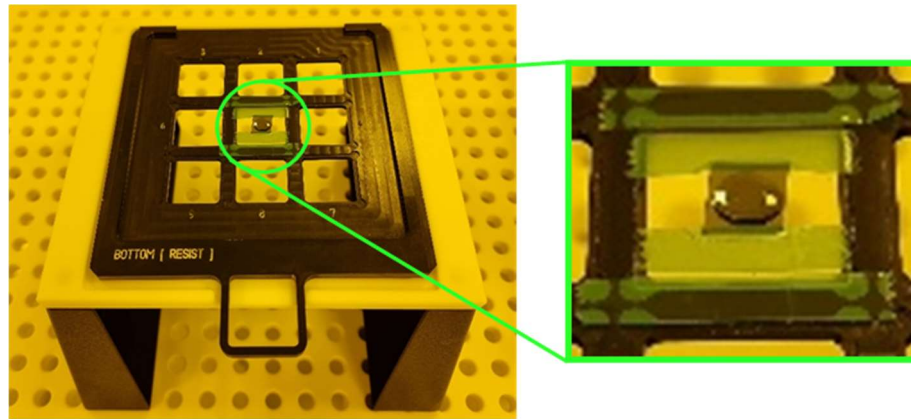
Figure 13. *Si substrate properly cleaned with a drop of photoresist and mounted on the sample holder, ready to be inserted in the laser printer.*

When the sample is placed inside the printer, the typical procedure is straightforward: approach the microscope objective slow until it enters the photoresist, focus the laser beam on the substrate, check tilt correction, load the fabrication file and start the fabrication job.

Once the fabrication is done, the structure needs to be developed in order to wash all the un-exposed photoresist over the structure and on the substrate. The development of the samples consists of three steps: first, a bath of propylene glycol methyl ether acetate or PGMEA (Microchemicals GmbH) for 30 min for IP-S and 20 min for IP-Dip; second, a bath of isopropanol of about 5 min; third, submersion of the sample in distilled H_2O (18.2 MΩ·cm) for 20 seconds approximately. After the submersion in water, it is possible to dry the substrate very gently with the nitrogen gun, but for sensitive structures, the sample dried in air. Note that the development times are not extremely critical, actually, keeping the sample for a much longer time in the developers would not change the structures properties significantly and it is a way to ensure that all the monomeric material is gone. As it can be imagined, is vital to treat the development process in a really careful manner, as the stress that the sample experience as well as the resist shrinkage in every step could easily damage the structure and alter its properties; that is the reason why it is washed with different solvents of different volatility and steps, as it minimizes the stress induced.
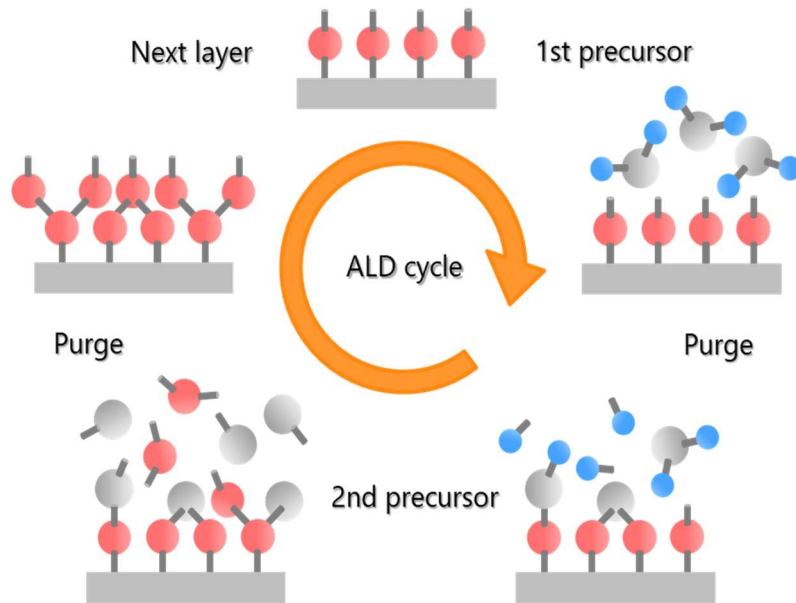
2.2 Atomic Layer Deposition

As it was described in previous sections, the realization of 3D metamaterials and study of its optical properties requires a higher effective refractive index other than the one of polymer. Additionally, the typical dimensions of meta-atoms are in the subwavelength order, which demands a precise control of the deposition thickness down to the nanometer scale. In order to achieve this, ALD is utilized for the ZnO coverage of the polymeric scaffolds. The basic principle of ALD and the chemistry involved in the deposition of ZnO are described in this chapter.

2.2.1 Working principle

ALD is a vapor-phase deposition technique that allows to synthetize ultra-thin films down to the atomic scale by repeating two subsequently executed half-cycles. This technique evolved originally from the chemical vapor deposition (CVD), where a film is deposited on a surface in consequence of a chemical reaction under vacuum. Despite that, ALD has superiority over CVD, as allows the use of very reactive precursors and thus a lower deposition temperature, crucial for coating polymeric structures. This fact is due to the sequential introduction of precursors into the growth chamber and the interruption of the cycles of precursor dosing by purging periods with inert gas, which make the reactants meet only at the surface of the growing film.[16,26]

The most common ALD process is based on two self-limiting surface reactions that deposit a binary compound film (see Figure 14). The first part of the cycle starts when the first precursor is introduced. The surface, already prepared to be reactive towards the precursor, starts the chemical interactions along the precursor until all anchors available on the surface are occupied and reaches saturation. Right after, it is required a purge step to wipe out the remaining unreacted precursor and byproducts that could have been created during the process. The purging is done by an inert gas, normally N_2. The second part of the cycle starts with the introduction of a second precursor, which reacts with the first precursor attached to the surface. Similar to the first half-cycle, the surface reaches cover saturation when the second precursor interacts with all the sites available of the first precursor attached to the surface and, as a result, these reactions lead to the desired product. Another purging is done before starting the next cycle for the same reason as above (to purge the byproducts and unreacted precursor).[26]
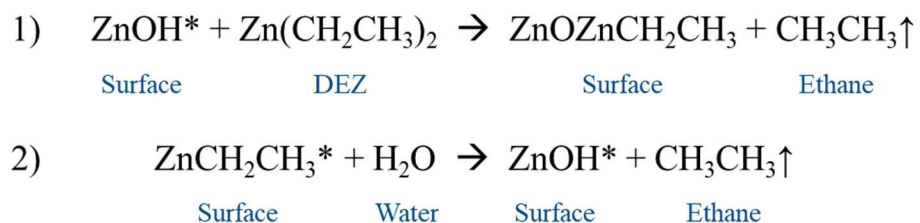
Figure 14. *Typical Atomic Layer Deposition (ALD) cycle.*

The atomic control of the deposited thickness in ALD is controlled by the number of total cycles performed, because, as mentioned, the chemistry involved is self-limiting. The term to refer to this growth rate is commonly called: growth per cycle (GPC).

2.2.2 Deposition of ZnO

The deposition of a layer of ZnO using ALD has been widely studied, thus, there are many precursor combinations and recipes to achieve diverse types of ZnO with different crystallography, thickness, adhesion to different substrates, etc. The precursors and recipe employed in this project were chosen taking into account the properties of the 3D polymer structures, such as the thermal stability, which does not allow extremely high temperature. These are well-known in the ALD community, as it is the most studied precursor combination: diethylzinc or DEZ ($Zn(CH_2CH_3)_2$) and water (H_2O). Thus, the aim in this section is to briefly describe the two reactions involved in the ALD process in order to understand the mechanism.[26]

The two self-terminating reactions for ZnO growth in ALD from DEZ and water take place as follows:

1) $\quad ZnOH^* + Zn(CH_2CH_3)_2 \rightarrow ZnOZnCH_2CH_3 + CH_3CH_3\uparrow$
    $\qquad$ Surface $\qquad\qquad$ DEZ $\qquad\qquad\qquad$ Surface $\qquad\qquad$ Ethane

2) $\qquad\quad ZnCH_2CH_3^* + H_2O \rightarrow ZnOH^* + CH_3CH_3\uparrow$
 $\qquad\qquad$ Surface $\qquad\quad$ Water $\quad$ Surface $\qquad$ Ethane

The first half-cycle ends with all the surface passivated by $ZnCH_2CH_3$ chemical groups. Then, there is the purge, which removes all the DEZ and ethane still present and, subsequently, the introduction of the second precursor to start the second half-cycle. In this step, water reacts with the passivated surface, producing again ethane as a byproduct, and the monolayer of ZnO is generated.[26]

2.2.3 Sample preparation and recipe

For this part, I acknowledge help of Dr. Krzysztof Mackosz with all the ALD depositions of ZnO on 3D metamaterials and advice and supervision of Dr. Ivo Utke during all coating steps.

The layers of ZnO were deposited in a custom-built stationary system for ALD using diethyl zinc (DEZ) precursor and water (H_2O) co-reactant. The optimal deposition temperature for the ZnO created by DEZ/water is still ambiguous compared to other precursor recipes. Temperature can vary between 100 and 170 °C.[27] However, as the polymeric scaffold structures in this project would have been probably damaged at 100 °C and above, the temperature chosen was 50 °C for the reactor walls and the sample, and room temperature for the reservoir. Such lowering of the temperature for this deposition is possible thanks to the high reactivity of DEZ.[28] Moreover, the deposition parameters were 0.1 s for precursor pulse, 1 s for exposure and 90 s for the purge in both cases (DEZ and water). The precursor pulse and the purge were executed with 15 sccm and 100 sccm argon flows, respectively.
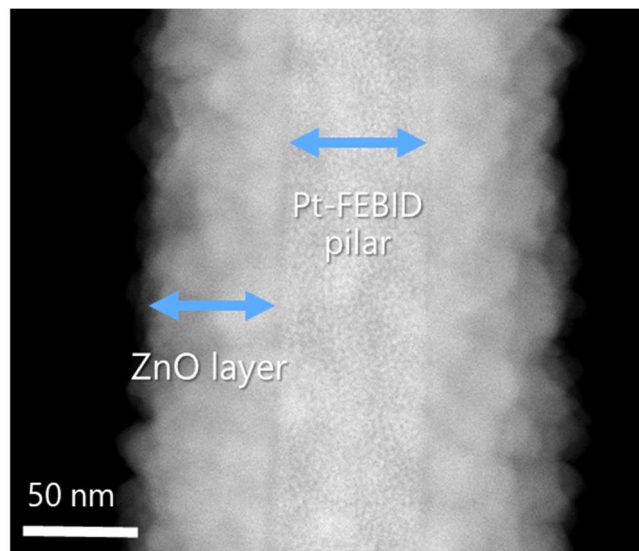
Figure 15. *Pt-FEBID grown pillar with a 60 nm ZnO layer. Image taken in the FEI Titan Themis 200 TEM using STEM mode.*

Furthermore, the number of cycles determined the overall thickness of the ZnO layer, which could be deducted from previous depositions of the group and calculations of the growth per cycle (GPC) in the recipe used at 50 °C. In our case, the depositions were about 60 and 80 nm, and the GPC was approximately 0.12 Å/cycle. During the ALD process, a Platinum FEBID (Focused electron beam induced deposition) grown pillar was placed on a TEM (Transmission Electronic Microscope) lift-out grid in order to measure the thickness of the ZnO layer deposited during the process. Afterwards, using STEM (Scanning TEM) mode in the FEI Titan Themis 200 (ThermoFisher) TEM, the thickness was directly measured with the image captured of the Pt-FEBID pillar (see Figure 15).

3. RESULTS AND DISCUSSION

In this chapter, the results and discussion of this work are presented. Each section describes one of the 3D metamaterials studied along the definition of its structure, the design optimization and structure characterization, the optical setup employed for its optical characterization, and the experimental measurements. Beforehand, some clarifications are worth mentioning.

The program used to design the structures was Blender 3.1.2, which allowed us to easily sketch and export the designs in the .stl format, essential for the loading of the structures into the Nanoscribe software.

The design optimization of the metamaterials was done in the aforementioned DeScribe software and the structural characterization was carried out in a high resolution field emission scanning electron microscope (SEM), more specifically the model Hitachi S-4800 (CFE).

Prior to the fabrication of each structure, tests were carried out in order to understand the importance of all the fabrication parameters and get used to the Nanoscribe Photonic Professional GT operation. These tests were performed with the unit cell of a well-known mechanical metamaterial (Kelvin foam), which was part of a side project (see Appendix for more detailed information).
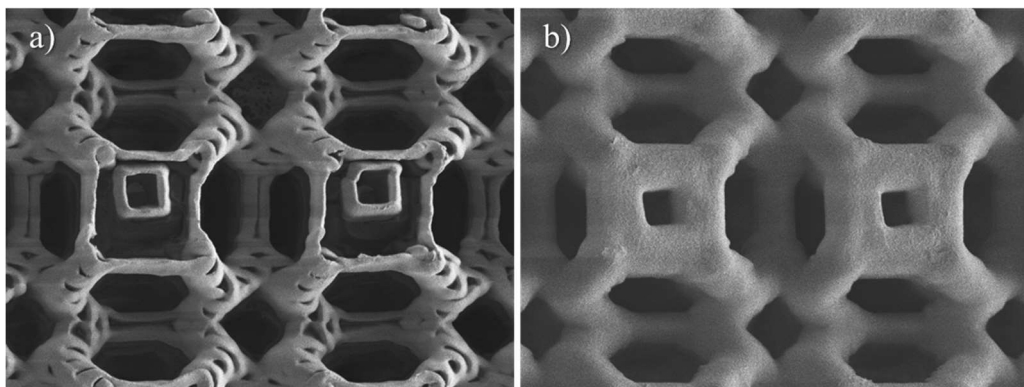
Figure 16. *SEM images of a 3D mechanical metamaterial design with different fabrication parameters.* ***a)*** *High slicing and contour distance values.* ***b)*** *Low slicing and contour distance values.*

As one can observe in Figure 16a and 16b, the meta-atom features vary depending on the parameters used, which, in this case, were the slicing and the contour distance the ones changed drastically to observe the effect. In general, for small values of slicing,

hatching and contour distance, the structure presents denser composition, and the opposite for high values. Hence, it is important to carry out a well-detailed study of the fabrication of microstructures by DLW, as the properties of the metamaterials can significantly vary depending on the fabrication parameters employed. These structures were fabricated with the 25x microscope objective and the IP-S photoresist, while the SEM images were taken with the emission current at 10 µA and the accelerating voltage at 1 kV; low voltage was necessary to avoid charging effects of nonconductive surfaces.

Additionally, the scan mode and the z-axis were tested. Qualitatively, the galvanometric and piezoelectric stage scan modules were the best choice for the scan mode and the z-axis, respectively. Therefore, all the fabricated metamaterials in this project have these two parameters set.

Furthermore, the electromagnetic characterization of the 3D metamaterials was carried out in different setups depending on the spectral regime in which the metamaterials have their electromagnetic resonances. The setups used in each case are shown and described in detail to understand the further results.

Prior to the experimental measurements, it was important to identify the thickness of the ZnO coating on top of a Si substrate. We estimated the thickness by checking optically the colour of our samples and compare it to the interference fringes for an incoming source of light (D65 standard daylight in this case). These calculations were executed in the free-to-use website "raacke.de" taking into account the materials involved (refractive index) and the thickness of the film.
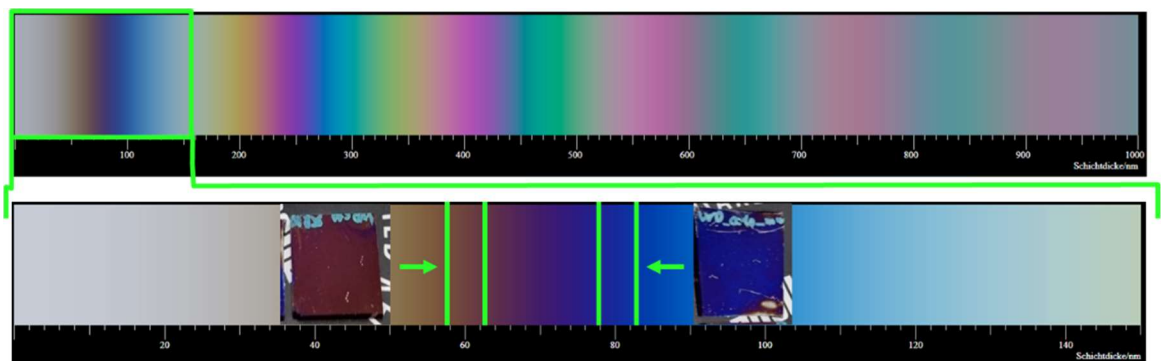
Figure 17. *Colour vs thickness simulation of a ZnO coating on top of a Si substrate. In the bottom panel, there are images of the WD samples on top of Si substrates for ZnO thicknesses of 60 nm and 80 nm, from left to right. This palette of colours is caused by the interference of light within the reflective substrate (Si) and the thin ZnO film.*

The colour of the samples was golden red and purplish blue, for the 60 nm and the 80 nm coating, respectively. As one can see in Figure 17, the WD samples on Si substrates in the inset images and the colours remarked in the bottom panel match each

other nicely, verifying once again that the film thicknesses achieved in these substrates were truly 60 nm and 80 nm. Note that for the SCR (THz) structure, the coating of the 80 nm ZnO had exactly the same colour as the WD sample (of 80 nm), as the two samples were coated in the same ALD chamber simultaneously.

3.1 Woodpile (VIS-NIR)

3.1.1 Structure

The so-called woodpile (WD) struc-ture, as its name indicates pile of wood, has layers of cylinders perpen-dicular to each other. Thus, the mod-elling consisted on the arrangement of different layers of cylinders placed one on top of the other in a perpendicular manner. The unit cell has a Face Cen-tered Cubic (FCC) structure as one can see in the cross-section of the metamaterial in Figure 18; the pattern repeats itself every 4 layers.
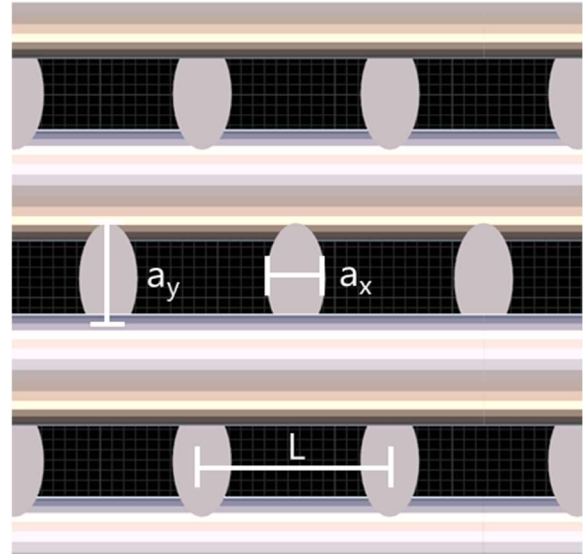

Figure 18. *Cross-section and dimensions of the WD structure as modelled in Blender.*

The size parameters a_x and a_y correspond to 500 nm and 1200 nm, respectively. L is the periodicity chosen in each case. For this project, periodicities ranging from 0.9 µm to 1.2 µm, in steps of 0.1 µm, were designed. These periodicities were chosen accordingly to a research study done by Serbin et al., where they demonstrated the fabrication of similar structures by two-photon polymerization technique presenting resonances in the near-infrared regime, which were shifted depending on the periodicity of the structure.[8] In that case, the pho-toresist employed was SU-8, which has higher refractive index as the one used in this project (Ip-Dip); that is the reason why they observed the resonances without any kind of coating. The parameters a_x and a_y were chosen taking into account the fabrication limitations of the DLW. The long-axis dimension of the cylinders and the height of the structure were selected depending on the size of the whole desired structure. We need structures large enough to achieve high stability and maintain its features during the fab-rication and development process. Therefore, the height was around 10 µm and the long axes (laterally) of the cylinders around 76 µm.

3.1.2 Design optimization and structure characterization

The WD structure was the most challenging fabrication and design optimization of this work, as it is the metamaterial with the smallest features; close to the limit of resolution of the Nanoscribe. For this reason, the first tests resulted in structures without the desired dimensions and destroyed or frayed due to their low mechanical stability; although the development of the samples is performed carefully, the stress during the development and drying process was enough to destroy the structures (see Figure 19a). In order to improve, I added walls surrounding the WD, so the structure could endure the stress (first test with walls shown in Figure 19b). After some trials, the structure was optimized inside the walls (see Figure 19c), however, as presented in Figure 19d, the cylinders were ruined near the walls due to the stretching of the cylinders attached to both sides. Thus, the next step was to fabricate the optimized WD (thicker cylinders) without walls, which turned out to be the final optimized version of the WD.
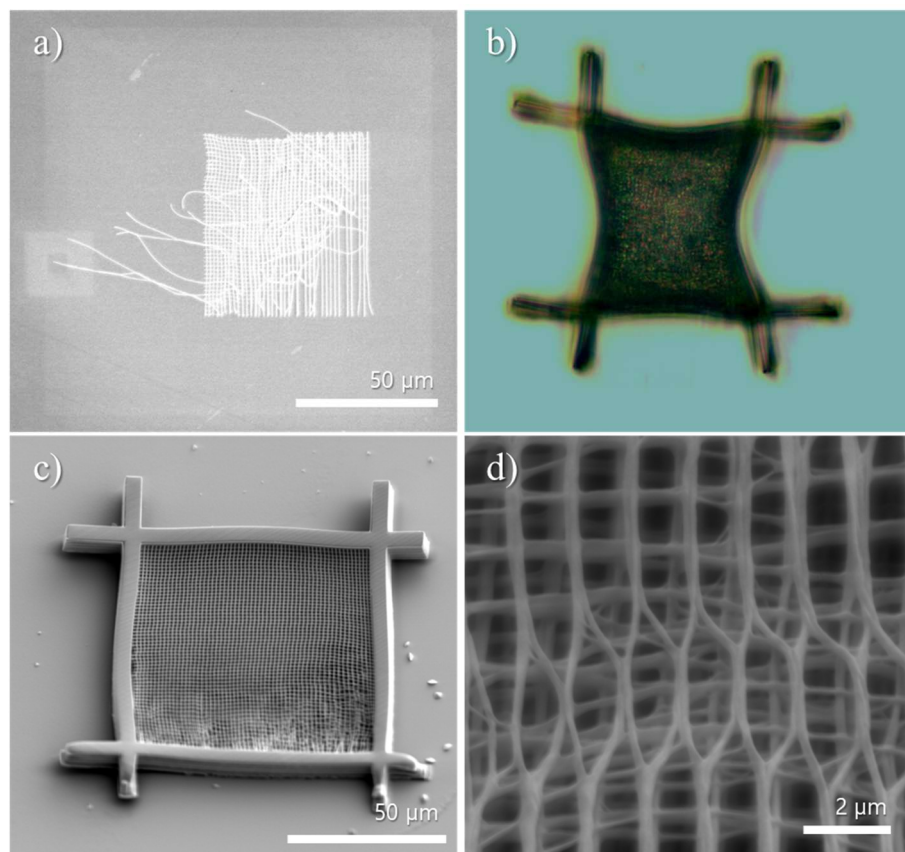
Figure 19. *SEM and optical images of the first fabrication tests for the WD structure. **a)** SEM image of the first WD frayed due to low mechanical stability. **b)** Optical microscope view of the first WD structure with walls. **c)** SEM image of the last test of the WD structure with walls. **d)** Close-up SEM image of c).*

The optimal WD design was performed with the fabrication parameters presented in Table 3, the 63x magnification microscope objective and the IP-Dip photoresist, as the limit resolution of the 25x objective is not enough to realize such small features. In order to achieve the dimensions desired along the use of the best resolution equipment, extremely low values for the fabrication parameters were chosen. These values, as one may notice, are below the resolution limits, thus, while fabricating, the actual voxel size was bigger than the one defined in DeScribe. In other words, the voxels were overlapped and, in that way, the desired features of the WD modelled were achieved with strong chemical and mechanical stability.
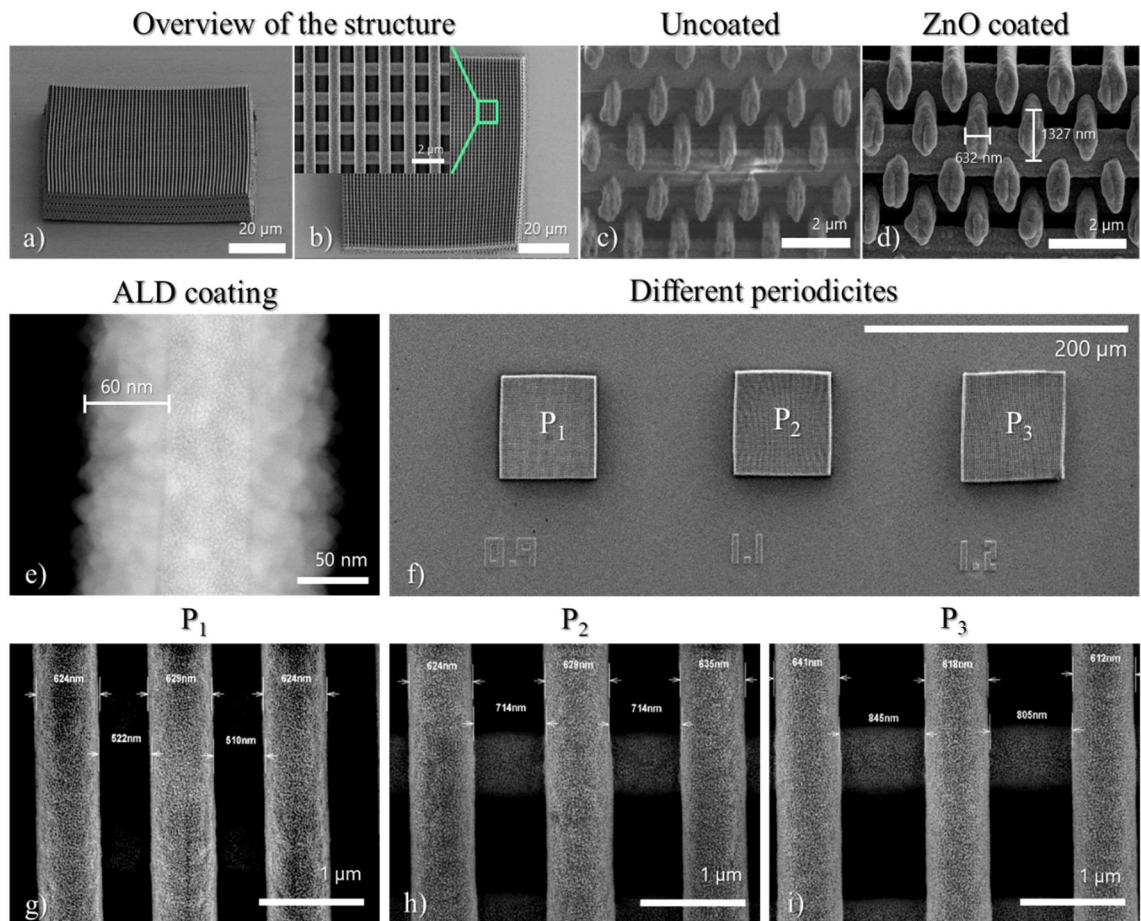
Table 3. *Optimized fabrication parameters for the WD design (structures shown in Figure 20).*

Parameter	Values
Slice (µm)	0.05
Fill mode	Solid
Hatching distance (µm)	0.05
Contour count	10
Contour distance (µm)	0.02
Base slice count	3
Hatching angle	120
Hatching angle offset	60
Scan mode	Galvo
Z-axis	Piezo

Figure 20 presents the structural characterization of the WD metamaterials. It can be observed that the structures were perfectly attached to the substrate and the cylinders were nicely arranged as in the modeled version (see Figure 20a and 20b). Then, the structures were coated with ZnO as explained in the methodology and, subsequently, characterized via SEM. Thanks to the ZnO coating, it was possible to increase the accelerating voltage for better quality images due to the conductivity of the ZnO, which is higher than the polymer. Thus, the SEM images of the uncoated structures were taken with the emission current at 10 µA and the accelerating voltage at 1 kV, while the coated structures were characterized with the same emission current and the accelerating voltage at 3 kV (see Figures 20c and 20d, where the uncoated SEM image has white spots related to charging effects). Additionally, in the coated image, one can validate that the dimensions of the cross section of the meta-atoms is approximately equal to the size

modelled plus the coating of the ZnO. Furthermore, the coating thickness was measured in the TEM with the Pt-FEBID fabricated pillar by taking an image in STEM mode (see Figure 20e) and two sets of samples with 60 nm and 80 nm coating thicknesses were produced. Regarding the design of different periodicities, they were not perfectly achieved; it is believed that the voxel size and the overlapping of this made the cylinders thicker, as well as having the coating of ZnO, thus, the periodicities were smaller than expected (see Figure 20f, 20g, 20h, and 20i). The 1.0 µm sample presented issues in the fabricated structure resulting in abnormal optical results, which is the reason it was decided to exclude this sample from the work. The periodicities for the 60 nm ZnO coating were approximately 516 nm, 714 nm, and 825 nm, while the ones for the 80 nm ZnO coating were approximately 552 nm, 745 nm, and 863 nm. From now on, the periodicities will be named P_1, P_2 and P_3, from shorter to larger.

Figure 20. *SEM structural characterization of the WD 3D metamaterials fabricated with the optimized parameters presented in Table 3 and TEM measurement. **a)** and **b)** Tilted and top views of the structure. Inset shows a zoom in photo of structure. **c)** and **d)** Tilted view of the uncoated and 60 nm ZnO coated WDs, respectively. **e)** Pt-FEBID fabricated pillar with a 60 nm ZnO layer seen with STEM mode in TEM. **f)** Top view of the different periodicities studied. **g)**, **h)** and **i)** High magnification top view of structures with P_1, P_2 and P_3, respectively.*

3.1.3 Optical setup (VIS-NIR)

The optical response in the VIS and NIR regimes of the WD structures was performed in a reconfigurable optical setup assembled by Dr. Angelos Xomalis (see Figure 21). This custom-built setup consists of: a QTH10/M - Quartz Tungsten-Halogen Lamp, focusing optics such as a pair of beam splitters, converging lenses and a MY50X-825 - 50X Mitutoyo Plan Apochromatic Objective (0.42 NA), a CS505CU - Kiralux 5.0 MP Colour CMOS Camera, and a QEPro spectrometer (300-900 nm range) and a NIRquest spectrometer (900-1700 nm range) from OceanInsight, which are operated with the software OceanView 2.0.8.
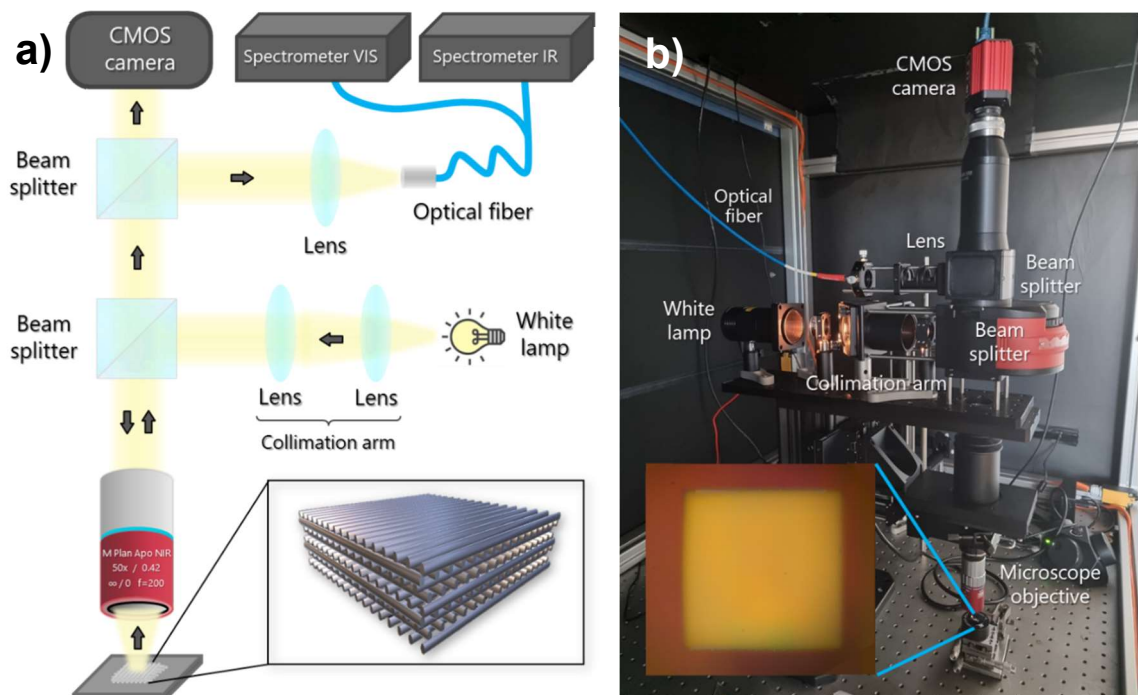
Figure 21. *The reconfigurable optical setup for spectroscopy measurements in the VIS-NIR regime. Consists of: Quartz Tungsten-Halogen Lamp, different focusing optics elements, a CMOS camera, one spectrometer for VIS, and one spectrometer for NIR. **a)** Sketch of the setup. **b)** A photo of the setup. Inset shows an optical microscope image of one of the WD structures.*

The aim of this setup is to characterize the reflection profile in both VIS and NIR regimes. In order to achieve it, the light of the Quartz Tungsten-Halogen Lamp is guided into the collimation arm and a beam splitter. From here, the beam splitter divides the beam towards a microscope objective tightly focusing onto the sample placed below and opposite another beam splitter. This second beam splitter separates the reflected beam again towards a CMOS camera, which allow us to see the sample, and a converging lens that focuses the beam into an optical fiber connected to the two spectrometers (VIS

and NIR). Thus, the light reflected back from the sample is collected for the CMOS camera and the optical fiber. When proceeding with the measurements, a normalization of the intensity counts gathered by the spectrometers is done, so that we have the right reflection profile of the samples. Note that the beam is equally illuminating all the metamaterial structure, hence, it is possible to measure the reflection of the overall structure from the top (see Figure 21, inset of the microscope image).

3.1.4 Experimental measurements

The woodpile structures were expected to have interesting reflection properties somewhere around the near-infrared region of the electromagnetic spectrum due to their periodicity, as Serbin et al. reported with similar structures and dimensions.[8] Thus, the reflection of the WD metamaterials was measured in the custom-built optical setup within 400 nm - 1600 nm range. All the data presented for each structure is the result of an average of 5 different measurements with acquisition time 1 s.

Prior to measurements, in order to ensure that the resonance wavelengths of the WD metamaterials were in the range of our spectrometers, basic calculations of these resonance wavelengths were carried out by utilizing the eq.1 presented in the theory chapter. For the square root of the permittivity, the refractive index of a ZnO film with 40 nm thickness ($\sqrt{\varepsilon}$ = n = 1.6141) was used, which was subtracted from the literature reported by Stelling et al.[29] The refractive index of the samples in this work should be slightly higher than the one reported, as they are thicker. Nevertheless, we note that the formula used is an approximation and it is employed here to give an idea of region of the electromagnetic spectrum should the resonances appear. Furthermore, the m value, which refers to the order of the resonance, was set to 2, as the first order of resonance for these structures turned to be out of the range of the spectrometers and the third order resonance, theoretically present in the visible regime, was too weak to be observed. Table 4 presents the resulting calculations for each sample and the measured resonances, where experimental periodicities and resonance wavelengths measured were subtracted from Figures 20 (SEM images) and 22 (reflection measurements), respectively.

Table 4. *Calculated and experimental data of the resonance wavelengths of the WD structures.*

ZnO coating (nm)	Sample	Periodicity measured (nm)	Resonance wavelength calculated (nm)	Resonance wavelength measured (nm)
60	P_1	516	833	1000
	P_2	714	1153	1080
	P_3	825	1332	1110
80	P_1	552	891	1045
	P_2	745	1202	1090
	P_3	863	1393	1130

As it can be observed, the calculated values for the resonance wavelengths are in the near-infrared regime where we can measure (833 nm to 1393 nm). Therefore, the next step was to measure in the optical custom-built setup.

Figure 22 shows a detailed study of the experimental reflection measurements obtained for the uncoated and ZnO coated WD metamaterials in the visible and near-infrared regimes.

The ZnO coated WD metamaterials present evident optical resonances in the 1000 nm - 1200 nm region, as one can observe in Figure 22d and 22f, which are inside the range calculated in Table 4, while the uncoated WD do not present any characteristic shape (see Figure 22b). For the 60 nm ZnO coated sample, there is a tendency in which the larger periodicities appear at longer wavelengths. The resonance for the P_1 structure has a characteristic dip at 1000 nm. Further, as the periodicity increases, the resonance shifts from 1000 nm to 1080 nm (P_2) and 1110 nm (P_3). The characteristic resonance of the P_1 structure could be caused by factors such as an error during the fabrication process or even a not perfectly aligned optical setup, which could affect the data near the limits of the spectrometer. In the case of the 80 nm ZnO coated sample, the periodicity-dependent optical resonances are even more recognisable and the shift between them gets more noticeable. The resonances follow a nice red-shift trend from 1045 nm to 1130 nm. Notice that, in any case, the WD metamaterials does not present remarkable effects or tendencies in the visible regime, where there should be the third order optical resonances but, as explained before, the intensity of these is too weak to detect.
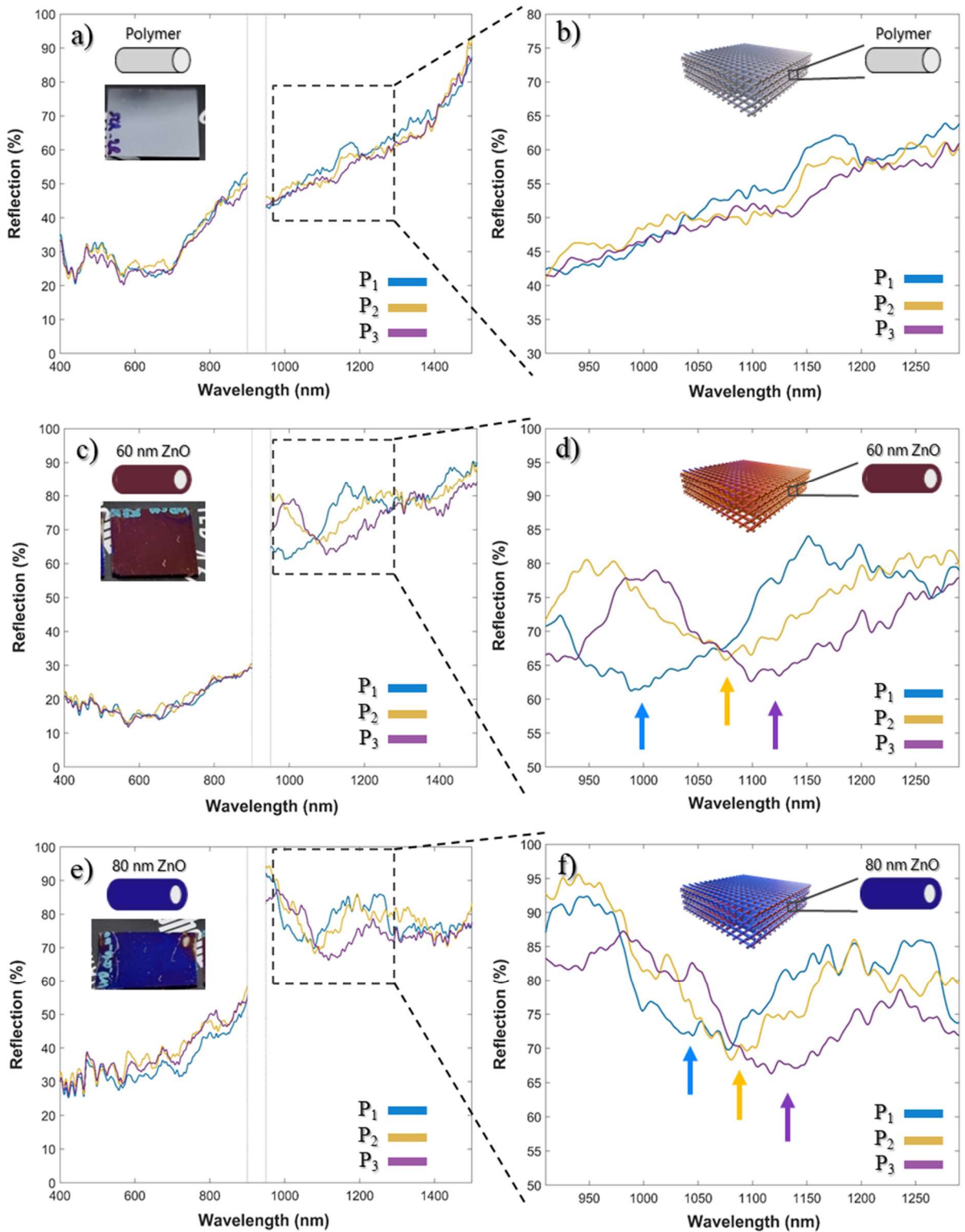
Figure 22. *Experimental reflection measurements of uncoated and ZnO coated WD metamaterials of different periodicities (P₁, P₂ and P₃) in the visible and near-infrared regime.* ***a)*** *Uncoated WD and* ***b)*** *Zoom-in.* ***c)*** *60 nm ZnO coated WD and* ***d)*** *Zoom-in.* ***e)*** *80 nm ZnO coated WD and* ***f)*** *Zoom-in. Insets show images of the whole samples (a, c, and e) and schematics of the WD structures (b, d, and f) with the characteristic colours of the ZnO layer determined by its thickness.*

The optical resonances of both ZnO coated samples are created by the geometry of the structure and its meta-atoms along with the effective parameters such as the effective refractive index (or effective permittivity) of the overall structure. The resonance wavelengths appear slightly at longer wavelength values for the 80 nm ZnO coated sample. This red-shift of the resonances of the 80 nm sample compared to the 60 nm sample is present in all the periodicities, and it is due to the increase of the thickness of the ZnO coating. The thicker coating implies more ZnO material on the WD, which translates to a higher effective refractive index red-shifting the resonance. As one can verify in eq.1, the increase of the effective refractive index influences directly the resonance wavelengths, appearing at longer wavelength values as demonstrated experimentally.
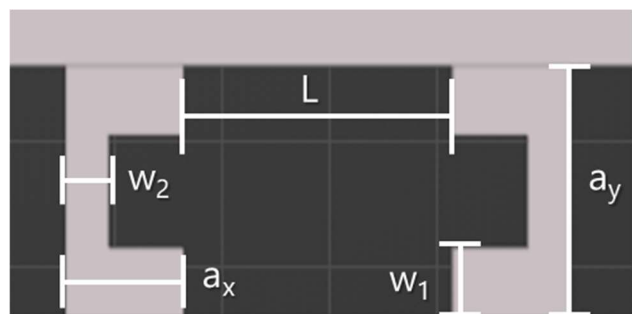
Another comparison between the samples is the increase of reflection in the range of 900 nm - 1200 nm when the samples are coated with ZnO. This last phenomenon was thought to be interesting enough to study it further and now it is part of future research (see Outlook).

3.2   Split-Cube Resonator (IR)

In this chapter, I acknowledge Dr. M. Manousidaki for the performance of the silver electroless plating on the Split-Cube Resonator (SCR) (IR) structures, as well as Dr. G. Kenanakis for the performance and analysis of the THz measurements carried out at the IESL-FORTH (Heraklion, Greece). This study is part of a publication (ACS Applied Optical Materials (2022) 10.1021/acsaom.2c00001), where I am co-author along the aforementioned scientists. In the work, a complete study of simulations of the SCR meta-atoms is presented, which are in agreement with the experimental results.[21]

3.2.1   Structure

The SCR meta-atom consists of a splitting cube in a C-shape form (see Figure 23) that can support a strong magnetic resonance with an incident magnetic field parallel to its long axis. Here the SCRs are grouped in pairs facing each other and there is only two layers perpendicular to each other, which is

Figure 23. *Cross-section showing the unit cell including dimensions of the SCR (IR) structure as modelled in Blender.*

the reason this structure is called two-layer inverted SCR geometry.[21]

The structural dimensions of the metallic metamaterial structures (see Figure 23) are as follows: a_x = 1.1 µm, a_y = 2 µm, w_1 = 0.55 µm, w_2 = 0.4 µm, and L = 2.5 µm.

3.2.2 Design optimization and structure characterization

The fabrication of the SCR (IR) was similarly challenging, as the desired features were close to the resolution limit of the Nanoscribe printer. The optimized design was performed with the fabrication parameters presented in Table 5. Here we not that the 63x magnification microscope objective and the IP-Dip photoresist are used to achieve the desired structural dimensions.

The design optimization was mainly based on the effect of the voxel overlapping explained in chapter 3.1. Although, the slicing had to be set quite large compared to the structure features, which can be clearly observed in Figure 24b. This fact is due to the meta-atom dimensions, which had to be achieved in order to observe the properties of the metamaterial found in the simulations study.[21] When using a smaller slicing value, the w_1 and w_2 dimensions could not be accomplished as consequence of the voxel size in the z-axis.

Table 5. *Optimized fabrication parameters for the SCR (mid-IR) structure (example shown in Figure 24).*

Parameter	Values
Slice (µm)	0.3
Fill mode	Solid
Hatching distance (µm)	0.05
Contour count	2
Contour distance (µm)	0.05
Base slice count	1
Hatching angle	120
Hatching angle offset	60
Scan mode	Galvo
Z-axis	Piezo

Furthermore, the SEM characterization (see Figure 24) was performed on an uncoated SCR (IR) optimized structure with emission current of 10 µA and accelerating voltage of 1 kV. As one can observe, high resolution images were achieved even though before the structures' metallization (Fig. X) as we sputter Au (~20 nm layer) to improve the quality of the SEM characterization and reduce the charging effects. Moreover, the

dimensions of the meta-atoms, shown in Figure 24b, are close to the modelled values. Thus, the IR characterization shows relatively good agreement with the simulations done previously.
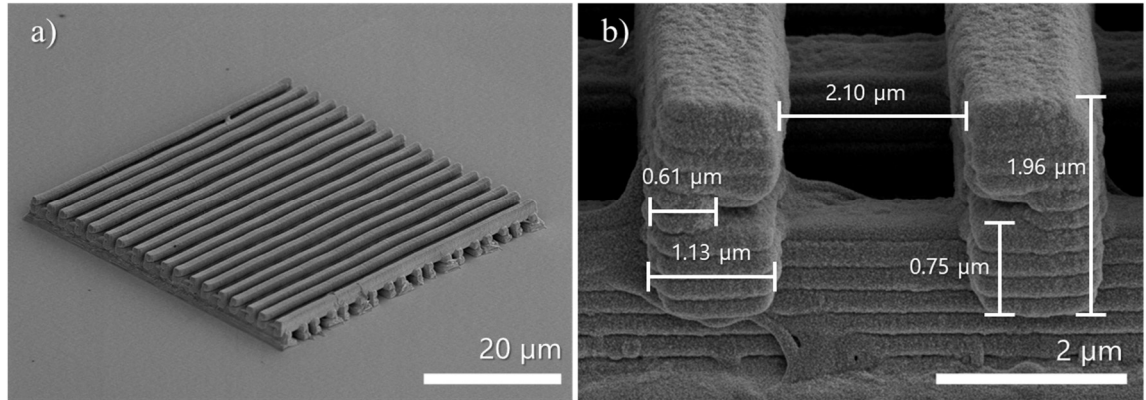
Figure 24. *SEM images of the Au coated (sputtered) SCR (IR) metamaterial with the optimized fabrication parameters presented in Table 5. **a)** Angle view of the structure. **b)** Cross-section of the unit-cell with all corresponding structural dimensions under high magnification inset.*

After the optimization design of the 3D polymeric structure, selective electroless silver plating is employed to cover the surface of the structure with Ag nanoparticles. This process utilizes exposed amino groups at the surface of the polymer to attract metal ions, resulting in nanoparticles after a reduction step.[30]

3.2.3 Characterization setup (IR)

In order to investigate the refractive index sensitivity in the IR regime of the SCR (mid-IR) metamaterial, reflectance measurements in air were performed with the aid of a Fourier-transform infrared spectrometer (Bruker Vertex 70v) attached to an infrared microscope (Bruker Hyperion 2000). Polarization-resolved measurements with a pair of ZnSe grid polarizers were carried out. To excite the magnetic dipole moments m_x in the first layer, the y linear polarization ($E = E_y\hat{\mathbf{y}}$) is used. Additionally, reflection measurements with an oil (Immersol 518F, n ~ 1.52) dropcasted onto the 3D-printed metamaterial were performed. The absorbed power spectrum was also extracted (see Figure 25). Finally, the experimental sensitivity ($\Delta\lambda/\Delta n$) of the 3D-printed metamaterial refractive index sensor is compared to the simulated predictions presented in the publication (see Ref 21 for more detailed information regarding the simulations).

3.2.4 Experimental measurements

Reflected and absorbed power spectrum measurements in air and oil for the SCR (mid-IR) metamaterial are shown in Figure 25.
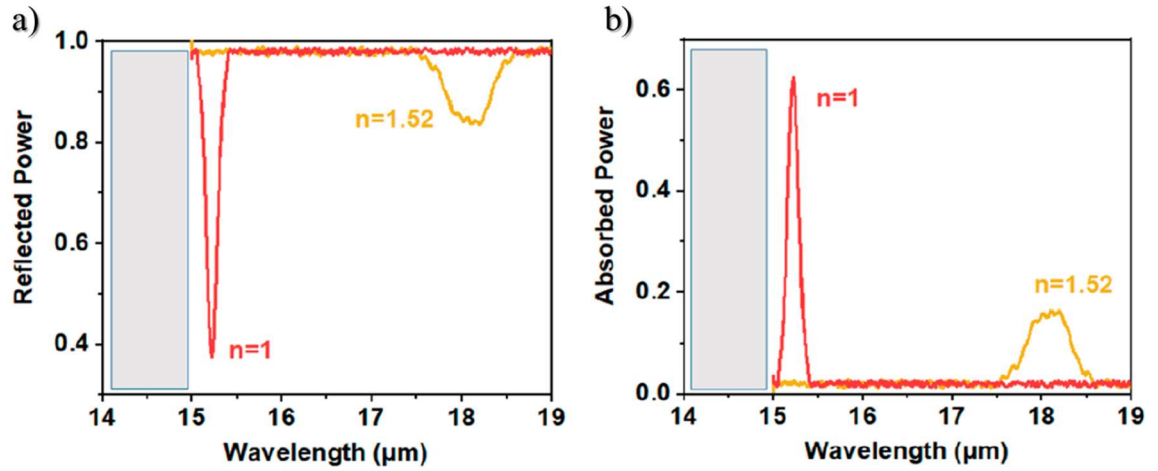
***Figure 25. a)** Experimental reflection measurements of SCR (IR) metamaterial covered with Ag nanoparticles. **b)** Calculated experimental absorbed power spectra in air (red) and oil (orange). The gray shaded box corresponds to the wavelengths where the detector is blind. Subtracted from Ref 21.*

The y linear polarization ($E = E_y \hat{y}$) employed to excite the magnetic dipole moments m_x of the first layer of meta-atoms and then coupled to the second layer resulting in enhanced light absorption; a sharp resonance appears at a wavelength of 15.2 μm (red, Figure 25). In addition, the resonance wavelength position, with the oil droplet, is shifted (by 2.8 μm) to longer infrared wavelengths, reaching 18 μm (orange, Figure 25). This agrees with the theoretical predictions assuming the dielectric environment around the metallic structure is increased. The resonance magnitude and Q-factor (quality factor) at 18 μm appear to be lower; an effect that we attribute to additional losses and coupling efficiencies that the oil used features at THz frequencies.

Furthermore, the experimental sensitivity ($\Delta\lambda/\Delta n$) of the SCR (mid-IR) metamaterial refractive index sensor is compared in Figure 26a to the simulated predictions (see Ref 21).
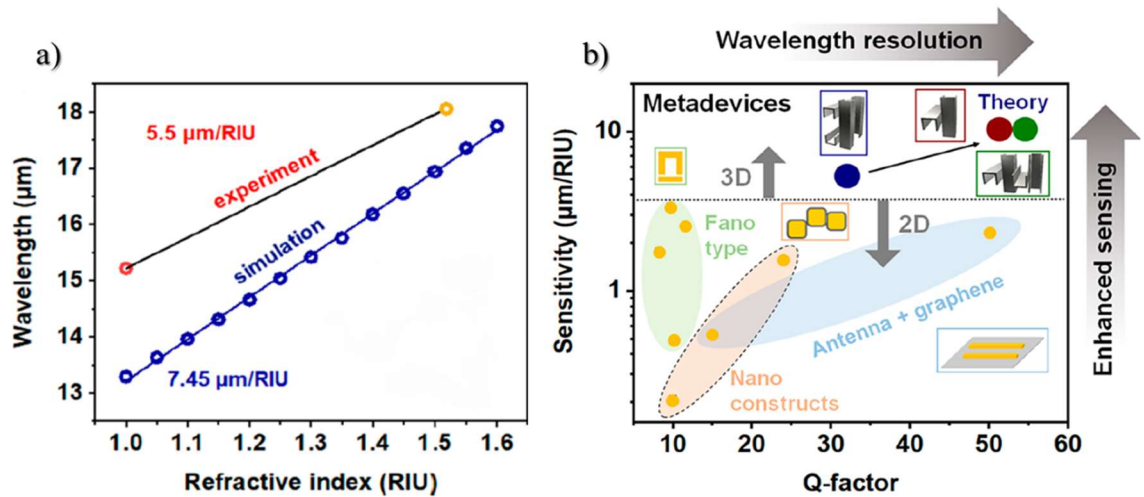
Figure 26. *a) Experimental (black solid) and simulated (blue solid) sensitivity Δλ/Δn (µm/RIU).* ***b)*** *Comparison of different metamaterial designs and nanophotonic constructs for refractive index sensing. High sensitivity results in larger resonance shifts, while high Q-factors offer better wavelength resolution in sensing. Subtracted from Ref 21.*

The experimental tested refractive indices were chosen to cover the entire simulated wavelength window (blue, Figure 26a). The experimental sensitivity follows the simulation trend allowing values as high as 5.5 µm/RIU (refractive index unit, RIU). The resonance position appears at somewhat longer wavelengths, which is due to fabrication imperfections as well as the difference in conductivity of the Ag nanoparticle-coated structures compared to the Ag bulk conductivity used in the simulations (see Ref 21 Methods). The high experimental sensitivity proves that the structures can be widely used for high-resolution refractive index sensing in challenging environments (extreme humidity and moisture) while their mechanical and chemical properties are preserved.

Finally, to highlight the potential of the technology presented, we compare its sensitivity with that of different metamaterial designs discussed in literature (see Figure 26b). These include structures showing Fano-type resonances (green, Figure 26b), hybrid antenna/graphene devices (blue), and nanophotonic constructs (orange, nanocubes and nanoprisms), operating in the visible, near-infrared, and mid-infrared regimes. Refractive index sensors must be selected according to their sensitivity (y-axis, Figure 26b), while increased Q-factors boost the wavelength resolution of the measurements (x-axis). The experimental data clearly show the potential of the 3D metamaterials fabricated for ultrasensitive refractive index detection. It is important to remark the 3D feature, as it is a key factor on the enhancement of the sensitivity. 3D structures have more surface and, consequently, more reactivity with the environment when compared to 2D structures, thus, they interact more with the surrounding molecules and their sensitivity is enhanced.

3.3 Split-Cube Resonator (THz)

In this chapter, I acknowledge Dr. Elena Mavrona for the development of the characterization THz setup, as well as the performance and analysis of the measurements carried out in the Empa of Dübendorf (Zurich, Switzerland). It is important to clarify that the results presented are preliminary measurements and, for future investigations, more detailed measurements and analysis are required to fully understand the metamaterial response.

3.3.1 Structure

Again, the Split-Cube Resonator meta-atom. In this case, the SCR are grouped in pairs facing each other and the overall structure has several layers. This unit cell is based on the research of Xomalis et al., where we report simulations of different arrangements of the SCR meta-atom.[21]
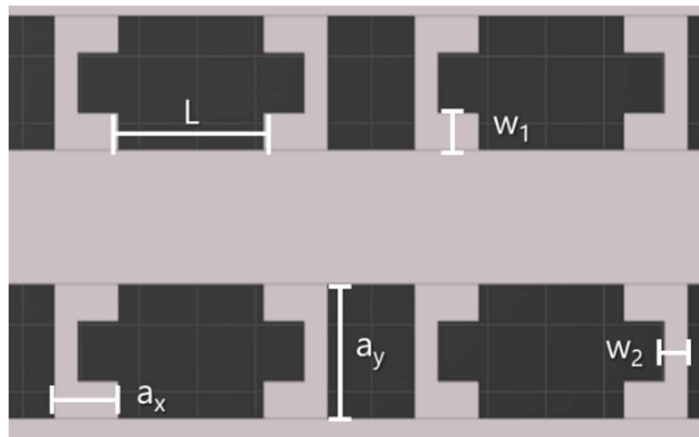
Figure 27. *Cross-section and dimensions of the SCR (THz) structure as modelled in Blender.*

The size parameters of this structure (see Figure 27) are a_x = 13 µm, a_y = 24 µm, w_1 = 6.5 µm, w_2 = 5 µm, and L = 30 µm. For an experimental demonstration of the electromagnetic response in the THz regime of this metamaterial, the sample should be able to accommodate the incidence beam, thus, the structure height was chosen to be 288 µm and the long axes 2000 µm.

3.3.2 Design optimization and structure characterization

The fabrication and optimization of the SCR (THz) metamaterial was much simpler than the other structures since this SCR was meant to act in the THz regime. The dimensions of the structure features were quite large, as presented above, thus, the microscope objective employed in this fabrication was the 25x magnification along the IP-S photoresist, while the parameters optimized were the ones presented in Table 6.

The design optimization was mainly based on the trade-off between the quality of the structure and the time of fabrication, as well as the best splitting parameters. On the one hand, the parameters were chosen accordingly with the time of fabrication without

compromising the realization of the features of the metamaterial; the optimized time resulted to be around 24 hours for this big structure (see Figure 28a). On the other hand, the splitting divided the structure in rectangular regions of 300 µm x 300 µm with an overlapping of 0.5 µm between regions. One clear example of the splitting effect can be seen in Figure 28d, together with the effect of the hatching, the contour count, and the contour distance parameters.

Table 6. *Optimized fabrication parameters for the SCR (THz) structure (example shown in Figure 28).*

Parameter	Values
Slice (µm)	0.5
Fill mode	Solid
Hatching distance (µm)	0.4
Contour count	4
Contour distance (µm)	0.5
Base slice count	10
Hatching angle	120
Hatching angle offset	60
Scan mode	Galvo
Z-axis	Piezo

The SEM characterization (see Figure 28) was carried out on the uncoated SCR (THz) structure with emission current of 10 µA and accelerating voltage of 1 kV. The reason why there is such excellent quality is due to the low magnification and the low accelerating voltage utilized; the electron beam was not tightly focused in a small area and no significant charging effects occurred. Furthermore, the dimensions of the meta-atoms and the unit cell is shown in Figure 28c and its inset, where, once again, can be verified that the modeled feature dimensions were almost perfectly achieved. For this metamaterial, only one set of samples was ZnO coated with 80 nm thickness. However, there is no figure showing the characteristics of the coated SCR (THz); this is due to the fact that the structure is quite large with respect to the 80 nm coating and thus not practically affecting the features of the metamaterial.
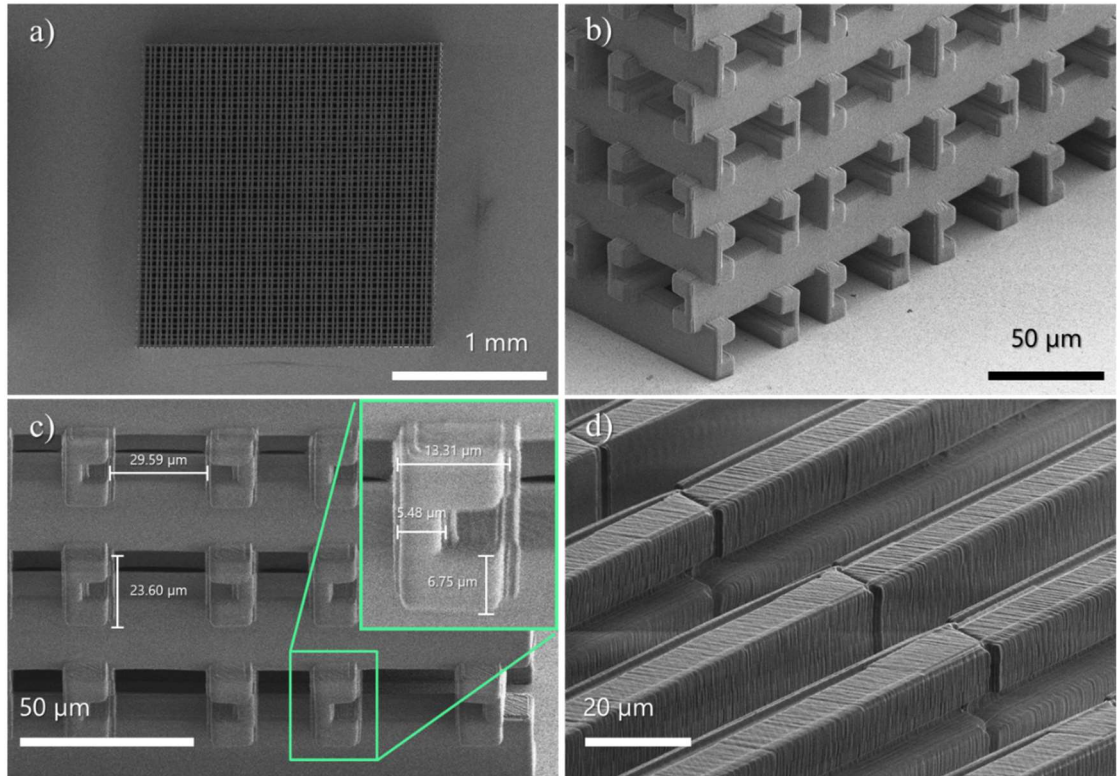
Figure 28. *SEM images of the uncoated SCR (THz) metamaterial with the optimized fabrication parameters presented in Table 6.* ***a)*** *Top view of the overall structure.* ***b)*** *Tilted view of the corner.* ***c)*** *Tilted view of the front and feature dimensions with high magnification inset.* ***d)*** *Tilted view close-up of the top showing the effect of the splitting mode.*

Once the structural characterization and the coating for the optimized design were finished, the sample was sent to Empa of Dübendorf (Zurich, Switzerland) for the electromagnetic characterization in the THz regime.

3.3.3 Characterization setup (THz)

The measurements in the THz regime were carried out in a conventional THz time-domain spectroscopy (THz-TDS) setup, a powerful tool for material characterization and the determination of the complex refractive index $ñ(w) = n(w) + ik(w)$.[31] In this project, the transmission of the SCR (THz) metamaterials was measured with a THz-TDS system based on a Ti:Sapphire laser (800 nm, 60 fs) and a pump-probe measurement scheme (see Figure 29).
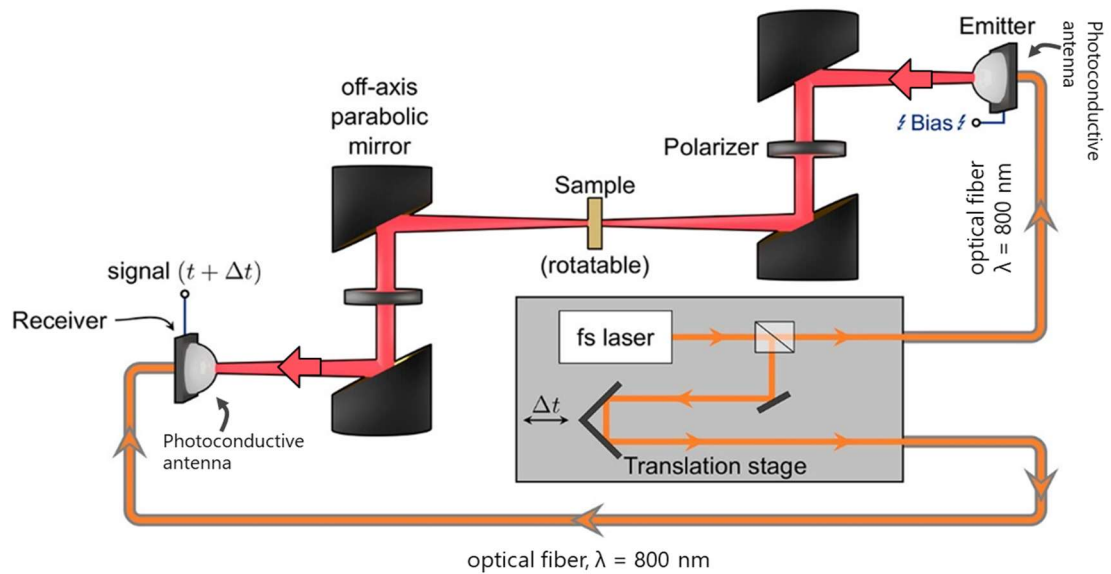
Figure 29. *Schematic of the THz time-domain spectroscopy (THz-TDS) setup employed for the characterization of the electromagnetic properties of the metamaterials in the THz regime. Subtracted from Ref 31.*

The generation of THz electromagnetic radiation is created when the fs pulsed laser reaches a photoconductive antenna; charges produced in the antenna, due to the incident laser beam, start to oscillate and, subsequently, re-radiate electromagnetic radiation that depends on the material of the antenna and the frequency of the laser, which corresponds to a range from 100 GHz to 3 THz in our case. Then, the THz radiation passes through the sample and reaches another photoconductive antenna, where a delay in time is measured. This delay contains the information about the transmission of the sample studied and can be extracted with the Fourier Transform. However, due to internal reflections in the transparent substrate, the data normally presents etalon-like interference pattern in this kind of measurements, but this can be substantially eliminated by making use of a time-window function.

As the SCR (THz) metamaterials of this project are subjected to study for asymmetric transmission, the system is designed in a way that the sample holder can be rotated. Thus, the THz waves' electric field direction (polarization), perpendicular to the surface of the sample, can be tuned to different angles ranging from 0° to 90°. Lastly, it is important to mention that this kind of metamaterials were fabricated on top of a high resistivity silicon substrate (HR-Si) which is more than 10 kΩ/cm in order to be transparent in the range of the electromagnetic spectrum of the measurements, where the metamaterials studied should have their characteristic asymmetric transmission properties.
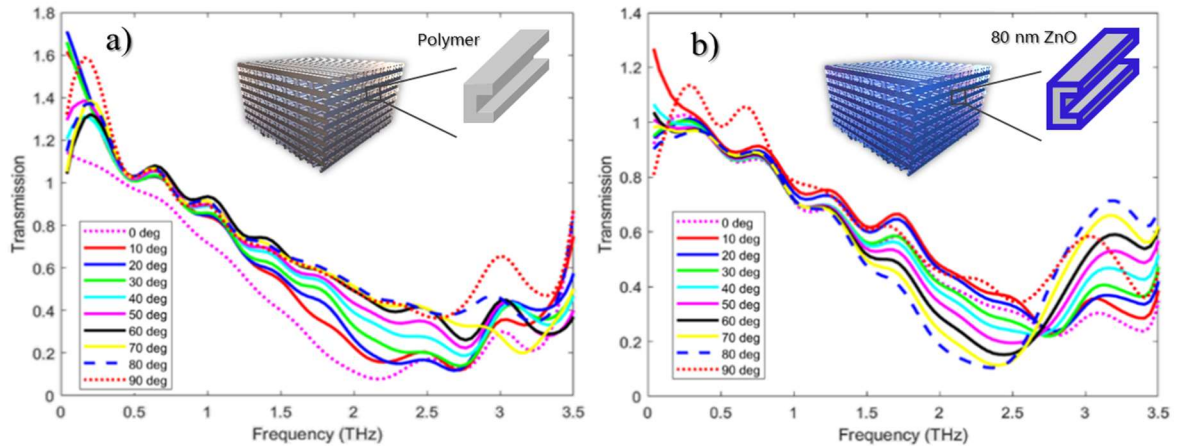
3.3.4 Experimental measurements

First step consisted in the measurement of the time delay of the radiation passing through the sample for different angles. It was decided to take data from 0 to 90 degrees in steps of 10, thus, in the case there is asymmetric transmission, the trend would be distinctly observed.
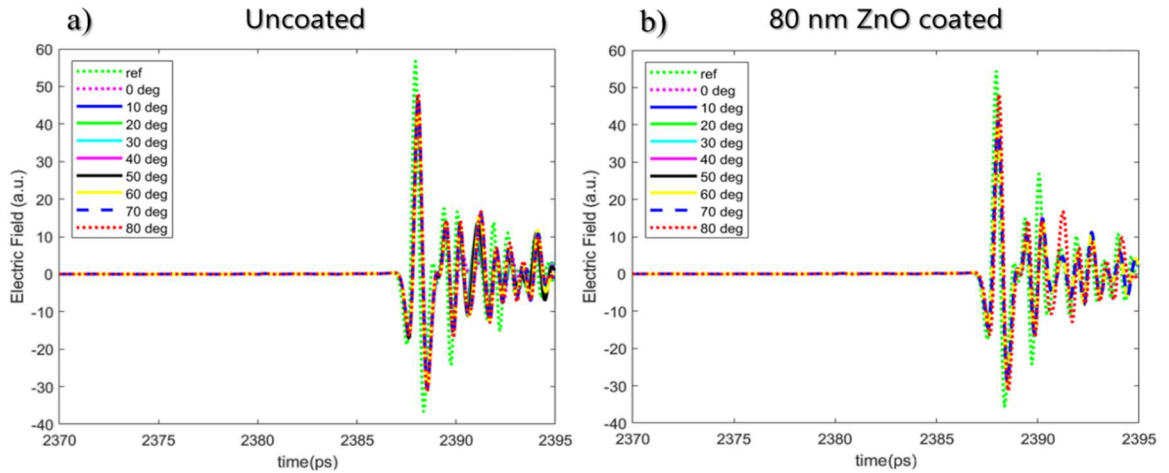
Figure 30. *Electric field vs time-delay measurements of uncoated and 80 nm ZnO SCR coated metamaterials.* **a)** *Uncoated SCR and* **b)** *80 nm ZnO coated SCR.*

Figure 30 presents the signal measured in the time domain for the different rotation angle for uncoated and 80 nm ZnO coated SCR (THz) metamaterials. As it can be seen, there is no clear information in these results and small oscillations appear due to the internal reflections of the substrate (etalon effect). Thus, next we apply a time-window function in order to reduce the etalon fringes of those internal reflections and further we apply a Fourier Transform to the data, which allows to go from the time-domain to the frequency-domain. In Figure 31, the transmission of both samples, uncoated and ZnO coated, is shown.

As it can be noticed in Figure 31, there is an evident trend followed in the two cases; as the structure is rotated, the resonance of the metamaterial becomes more intense and, consequently, the transmission gets lowered in the region of the spectrum where the resonance takes place, which in both cases is between 3.0 THz and 3.5 THz approximately, as seen in the preliminary simulations (see Appendix). However, similar to the WD study, it is obvious that the coated structure has a more defined profile, and the resonances are more prominent, which is again due to the increase of the effective refractive index. Nevertheless, in the coated SCR (THz), it can be observed that the 90 degrees measurement is not following the tendency of the other measurements; the reason of it is unknown and there is not enough data to make any statement.

Figure 31. *Experimental transmission measurements of uncoated and 80 nm ZnO coated SCR (THz) metamaterials in the THz regime.* ***a)*** *Uncoated and* ***b)*** *80 nm ZnO coated SCRs. Insets show schematics of the SCR units and structures. Note that the colours of both plots are inverted, but the 0 degrees in a) is equal to the 90 degrees in b), and vice versa.*

Here the ZnO coated structures will facilitate different resonances from the one discussed before utilising metallic coatings.[21] If the structure is conductive then the incoming electromagnetic wave (when polarized along perpendicular to the long axis) will induce magnetic dipole moments that will induce other dipole moments to the next layer below as they are physically connected. However, as the dipole moment of the consecutive layer showing the opposite direction will cancel each other. This can either lead to asymmetric transmission for counter propagating beams or perfect radiation absorption. However, here we utilize dielectric coating (ZnO) thus the expected resonances are based on displacement volumetric dipoles (as normal dielectric metamaterial resonances) and not oscillating surface current (conductive/metallic metamaterials). For understanding this better, we are now performing detailed full-wave calculation to support future investigations.

4. CONCLUSIONS

In this work, three-dimensional (3D) metamaterial structures with enhanced electromagnetic properties in the near-, mid- infrared and THz spectrum regimes were presented.

First, Woodpile-based (WD) structures were fabricated to study the periodicity-dependent optical properties of this metamaterial. The design and fabrication of the WD were optimized and characterized with high-resolution SEM. Furthermore, two sets of structures were coated with 60 and 80 nm thickness ZnO layer employing the Atomic Layer Deposition (ALD) technique, and optically characterized in a custom-built optical microscope. The reflection measurements for both coated set of WDs presented optical resonances in the near-infrared regime as well as red-shifted resonances for the thicker coatings, as expected.

Further, a Split-Cube Resonator (SCR) based structure was fabricated as a refractive index sensor in the mid-IR regime. Similar to the procedure for the WD, the design and fabrication were optimized and characterized with high-resolution SEM. Further, the structure was covered with Ag nanoparticles by selective electroless silver plating, and electromagnetically characterized in the mid-IR regime in a commercial Fourier-transform infrared spectrometer under two different refractive index environments. The reflected and absorbed power spectrum curves showed resonances when the metamaterial was surrounded by air and oil, presenting a red-shift in the case of the oil, where the refractive index was higher. Additionally, the experimental sensitivity followed the simulation trend allowing values as high as 5.5 μm/RIU. Thus, we proved that the 3D SCR (mid-IR) clearly shows potential for ultrasensitive refractive index detection in challenging environments, while its mechanical and chemical properties are preserved.

Moreover, another SCR based structure was studied acting in the THz regime as an asymmetric transmission device. Analogous to the previous structures, the design and fabrication of the SCR (THz) metamaterial were optimized and characterized with SEM. Then, the structure was coated with an 80 nm ZnO layer using the ALD technique, and electromagnetically characterized in a custom-built THz time-domain spectroscopy (THz-TDS) setup. The results demonstrated asymmetric transmission from 0 to 90 degrees in the THz domain by the uncoated and coated SCR (THz) structures. The ZnO coated structures showed stronger light-matter interactions and resonances due to the higher effective refractive index.

It was experimentally demonstrated that the proposed 3D structures can be easily fabricated with Direct Laser Writing (DLW) and coated with ALD technique, presenting high mechanical and chemical stability. This enables the use of such metamaterials in a wide range of applications reaching from narrow filters and optical switches to direction selective absorbers and isolators. The proposed printing technique and conformal deposition recipes are ideal candidates for the fabrication of complex 3D metamaterial designs in a extensive variety of operation wavelengths. Thus, the work presented here should be effective in providing guidance for the performance of metamaterial structures and its integration with technologies focusing on enhanced sensing, imaging, energy harvesting and photovoltaics. Further investigations may concern the deep theoretical study of WD and SCR (THz) structures, the coating of structures with other materials compatible with ALD technique, and the experimental large-scale fabrication of SCR (mid-IR) that allows easy integration of such IR metamaterial-based optics (waveplates and absorptive filters) with standard infrared setups, i.e., FT-IRs and quantum cascade lasers.

In addition, I also worked on a side project (see Appendix) involving the fabrication of 3D mechanical metamaterials coated with ZnO that show extreme robustness and flexibility that such brittle materials don't have normally. This shows great potential for the nanofabrication of biomimetic tissues as the proposed metamaterials' mechanical properties cover a wide range of natural biomaterials.

5. OUTLOOK

Besides the investigations mentioned in the previous section, here we discuss on potential future research related to the WD structures. Thus, in this section, we show preliminary results of the ZnO coated WD metamaterials.

5.1 ZnO coated WD reflection enhancement

As seen in chapter 3.1, the ZnO-coated WD structures exhibit an increase in the reflection in some parts of the spectrum (Figure 22 results of WD). After observing this, it was decided to repeat the reflection measurements without normalization in order to check the total number of counts for all structures. Note that the experimental data shown in this section is measured in the VIS regime, as the NIR regime did not exhibit any remarkable changes.

Here, we measured the white source reflection from a silver mirror, a Si substrate, and ZnO layers deposited on a Si substrate with thicknesses ranging from 20 nm to 160 nm(see Figure 32a). Furthermore, we measured a 60 nm ZnO layer on top of a Si substrate (green) and then 60 nm ZnO coated WD structures with different periodicities (see Figure 32b). All the mentioned measurements were performed without normalization.
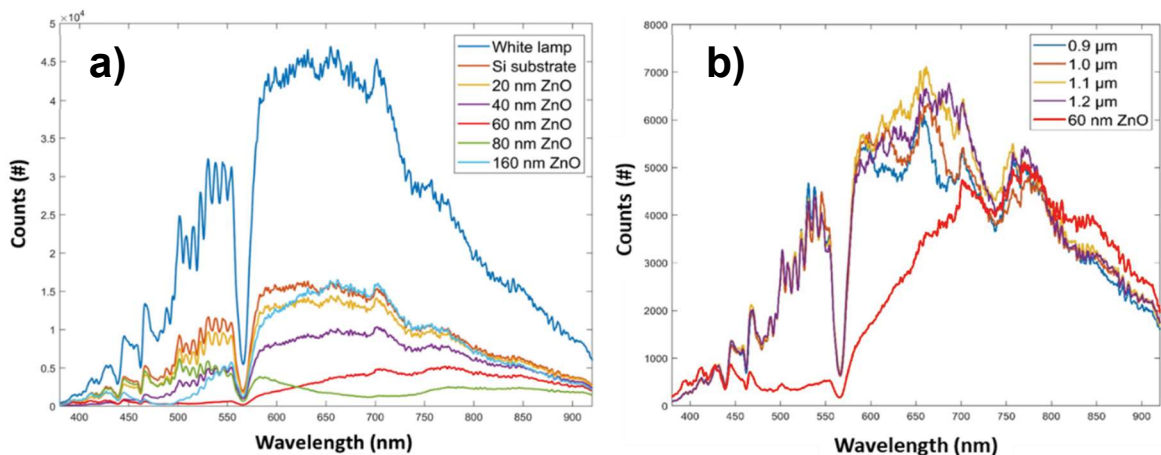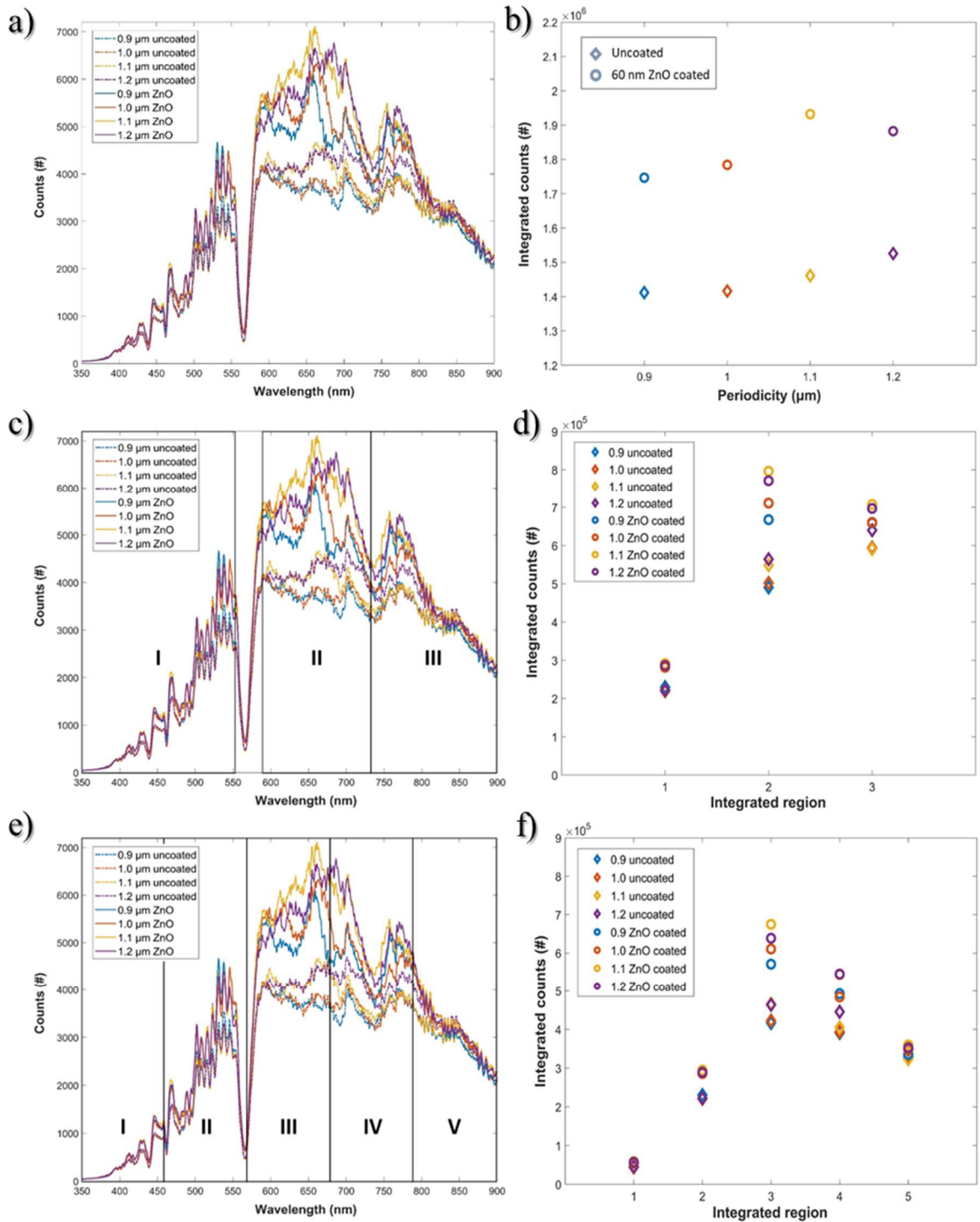

Figure 32. *Experimental reflection measurements without normalization. **a)** White source used in the measurements, a Si substrate, and ZnO layers of different thicknesses (20, 40, 60, 80, 160 nm) on top of a Si substrate. **b)** 60 nm ZnO layer deposited on a Si substrate and 60 nm ZnO coated WD structure of different periodicities (0.9, 1.0, 1.1 and 1.2 µm) throughout the visible regime.*

The experimental measurements in Figure 32a show the decrease of reflection of the ZnO layers as the thickness increases until it reaches 160 nm, where the reflection returns back to the initial values. This phenomenon is a consequence of the ZnO layer being deposited on top of a Si substrate, which act as a Fabry-Pérot cavity and that is the reason of the colours seen in Figure 17. We note that a dip at around 570 nm appears in all cases. This dip was observed in all the measurements without normalization, and it is caused by the white source used in the experiments. The reflection measurements in Figure 32b show that the coated WD structures exhibit higher reflection than the flat ZnO layer. The 60 nm ZnO layer has a peak between 600-900 nm, which is agreement with the golden red colour that the substrate presents macroscopically. Next, Figure 33 presents the reflection measurements of the WD structures (uncoated and 60 nm ZnO coated) without normalization.

As it can be observed in Figure 33, the 60 nm ZnO coated WD metamaterials present higher reflectivity in the majority of the measured visible regime. In order to proceed with a complete study and understand this phenomenon, the reflection measurements for each sample were integrated to subtract the area under the curves and analyse quantitatively the results.

Figure 33b shows the enhancement of reflection when the WD metamaterials are ZnO coated (circles) compared to the uncoated structures (diamonds). Furthermore, Figures 33d and 33f show the integrated areas under the reflection curves divided in regions, as the change in reflection does not seem the same in throughout the visible spectrum. In both cases, the central region of the measured spectrum (between 600-750 nm approximately) exhibit a higher increase of the reflection. Moreover, the ZnO coated WD have different reflection values depending on the periodicity of the structure, being the 1.1 µm WD the highest one.

Figure 33. *Experimental reflection measurements without normalization of uncoated and 60 nm ZnO coated WD metamaterials of different periodicities (0.9, 1.0, 1.1 and 1.2 µm) throughout the visible regime. a), c) and e) present uncoated (dashed) and coated (solid) WD structures of different periodicities. b), d) and f) present the integrated area values from the reflection curves on a, c and e, respectively. The diamonds stand for the uncoated structures and the circles, for the coated ones. Lines in c and e indicate the different regions that were integrated.*

Finally, another analysis of the results was performed to observe the percentage of reflection increase of the coated structures over the uncoated (see Figure 34).
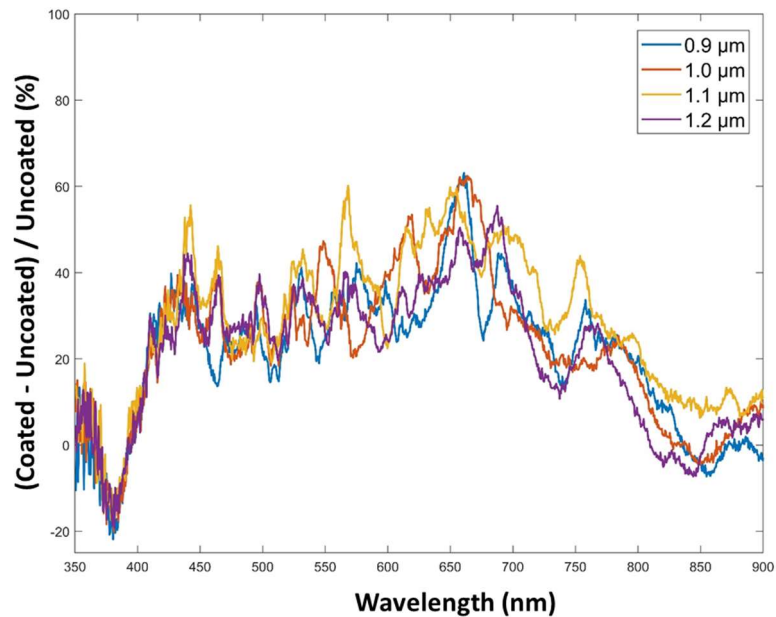
Figure 34. *Percentage increase of the reflection values of the 60 nm ZnO coated WD structures over the uncoated for different periodicities (0.9, 1.0, 1.1 and 1.2 µm) throughout the visible regime.*

As one can observe, the coated WD structures have an increase of reflection of around 30 % in the majority of the spectrum and they reach values around 60 % between 650 nm and 700 nm, which agrees with the results discussed above.

Based on the experimental results presented in this section, it can be concluded that the structure of the WD is enhancing the reflectivity and could be periodicity-dependent. It is believed that this phenomenon arises from the (high order) resonances of the WD as metamaterials). However, this discussion requires a more detailed study which may concern a theoretical study of the ZnO coated structures, as well as extra experimental measurements with different periodicities and coating thicknesses.

LIST OF REFERENCES

1   Chikkaraddy, R., Xomalis, A., Jakob, L. A. & Baumberg, J. J. Mid-infrared-perturbed molecular vibrational signatures in plasmonic nanocavities. *Light: Science & Applications* **11**, 19 (2022). https://doi.org:10.1038/s41377-022-00709-8

2   Xomalis, A. *et al.* Detecting mid-infrared light by molecular frequency upconversion in dual-wavelength nanoantennas. *Science* **374**, 1268-1271 (2021). https://doi.org:10.1126/science.abk2593

3   Liu, Y. & Zhang, X. Metamaterials: a new frontier of science and technology. *Chemical Society Reviews* **40**, 2494-2507 (2011). https://doi.org:10.1039/C0CS00184H

4   Tsilipakos, O. *et al.* Split-cube-resonator-based metamaterials for polarization-selective asymmetric perfect absorption. *Scientific Reports* **10**, 17653 (2020). https://doi.org:10.1038/s41598-020-74221-7

5   Kenanakis, G. *et al.* Three-Dimensional Infrared Metamaterial with Asymmetric Transmission. *ACS Photonics* **2**, 287-294 (2015). https://doi.org:10.1021/ph5003818

6   Lin, S., Moreno, J. & Fleming, J. Three-dimensional photonic-crystal emitter for thermal photovoltaic power generation. *Applied Physics Letters* **83**, 380-382 (2003). https://doi.org:10.1063/1.1592614

7   Fleming, J. G., Lin, S. Y., El-Kady, I., Biswas, R. & Ho, K. M. All-metallic three-dimensional photonic crystals with a large infrared bandgap. *Nature* **417**, 52-55 (2002). https://doi.org:10.1038/417052a

8   Serbin, J., Ovsianikov, A. & Chichkov, B. Fabrication of woodpile structures by two-photon polymerization and investigation of their optical properties. *Optics Express* **12**, 5221-5228 (2004). https://doi.org:10.1364/OPEX.12.005221

9   Vasilantonakis, N. *et al.* Three-Dimensional Metallic Photonic Crystals with Optical Bandgaps. *Advanced Materials* **24**, 1101-1105 (2012). https://doi.org:https://doi.org/10.1002/adma.201104778

10   Fischer, J. & Wegener, M. Three-dimensional direct laser writing inspired by stimulated-emission-depletion microscopy [Invited]. *Optical Materials Express* **1**, 614-624 (2011). https://doi.org:10.1364/OME.1.000614

11   Rill, M. S. *et al.* Photonic metamaterials by direct laser writing and silver chemical vapour deposition. *Nature Materials* **7**, 543-546 (2008). https://doi.org:10.1038/nmat2197

12   Dorsey, K. J. *et al.* Atomic Layer Deposition for Membranes, Metamaterials, and Mechanisms. *Advanced Materials* **31**, 1901944 (2019). https://doi.org:https://doi.org/10.1002/adma.201901944

13   Zhang, J., Li, Y., Cao, K. & Chen, R. Advances in Atomic Layer Deposition. *Nanomanufacturing and Metrology* **5**, 191-208 (2022). https://doi.org:10.1007/s41871-022-00136-8

14   Özgür, Ü. *et al.* A comprehensive review of ZnO materials and devices. *Journal of Applied Physics* **98**, 041301 (2005). https://doi.org:10.1063/1.1992666

15 Giakoumaki, A. N. *et al.* 3D micro-structured arrays of ZnO nanorods. *Scientific Reports* **7**, 2100 (2017). https://doi.org:10.1038/s41598-017-02231-z

16 Guziewicz, E. *et al.* Extremely low temperature growth of ZnO by atomic layer deposition. *Journal of Applied Physics* **103**, 033515 (2008). https://doi.org:10.1063/1.2836819

17 Chawla, V. *et al.* Fracture Mechanics and Oxygen Gas Barrier Properties of Al2O3/ZnO Nanolaminates on PET Deposited by Atomic Layer Deposition. *Nanomaterials* **9** (2019). https://doi.org:10.3390/nano9010088

18 Lujala, V., Skarp, J., Tammenmaa, M. & Suntola, T. Atomic layer epitaxy growth of doped zinc oxide thin films from organometals. *Applied Surface Science* **82**-**83**, 34-40 (1994). https://doi.org:https://doi.org/10.1016/0169-4332(94)90192-9

19 Kadic, M., Milton, G. W., van Hecke, M. & Wegener, M. 3D metamaterials. *Nature Reviews Physics* **1**, 198-210 (2019). https://doi.org:10.1038/s42254-018-0018-y

20 Liu, H. *et al.* High-Order Photonic Cavity Modes Enabled 3D Structural Colors. *ACS Nano* **16**, 8244-8252 (2022). https://doi.org:10.1021/acsnano.2c01999

21 Xomalis, A. *et al.* Enhanced Refractive Index Sensing with Direction-Selective Three-Dimensional Infrared Metamaterials. *ACS Applied Optical Materials* (2022). https://doi.org:10.1021/acsaom.2c00001

22 Wesche, R. *Springer Handbook of Electronic and Photonic Materials*. (Springer International Publishing, 2017).

23 Selimis, A., Mironov, V. & Farsari, M. Direct laser writing: Principles and materials for scaffold 3D printing. *Microelectronic Engineering* **132**, 83-89 (2015). https://doi.org:https://doi.org/10.1016/j.mee.2014.10.001

24 GmbH, N. *Photonic Professional (GT) User Manual*. (2017).

25 Micro-Nano-Technology, C. o. *Describe: Getting started Manual*, 2019).

26 Shkondin, E. *Fabrication of Hyperbolic Metamaterials using Atomic Layer Deposition* PhD Thesis thesis, Technical University of Denmark, (2016).

27 Guziewicz, E. *et al.* ALD grown zinc oxide with controllable electrical properties. *Semiconductor Science and Technology* **27**, 074011 (2012). https://doi.org:10.1088/0268-1242/27/7/074011

28 E. Guziewicz *et al.* Extra-Low Temperature Growth of ZnO Thin Films by Atomic Layer Deposition *Journal of the Korean Physical Society* **53**, pp. 2880~2883 (2007).

29 Stelling, C. *et al.* Plasmonic nanomeshes: their ambivalent role as transparent electrodes in organic solar cells. *Scientific Reports* **7**, 42530 (2017). https://doi.org:10.1038/srep42530

30 Sakellari, I. *et al.* 3D Chiral Plasmonic Metamaterials Fabricated by Direct Laser Writing: The Twisted Omega Particle. *Advanced Optical Materials* **5**, 1700200 (2017). https://doi.org:https://doi.org/10.1002/adom.201700200

31 Zeng, Z. *et al.* Terahertz Birefringent Biomimetic Aerogels Based on Cellulose Nanofibers and Conductive Nanomaterials. *ACS Nano* **15**, 7451-7462 (2021). https://doi.org:10.1021/acsnano.1c00856

APPENDIX

Preliminary simulations of SCR (THz)

In this section, I acknowledge Dr. Odysseas Tsilipakos for the performance of the simulations carried out at the IESL-FORTH (Heraklion, Greece).

Preliminary simulations of the SCR (THz) without coating and considering HR-Si substrate were carried out. These simulations considered a refractive index of 1.5 for the polymer scaffold and a refractive index of 3.5 for the HR-Si, whose thickness was 400 μm. For the structure, different number of unit cells were considered in order to see at which number of unit cells (Ncells in Figure A1) the resonances were appearing.
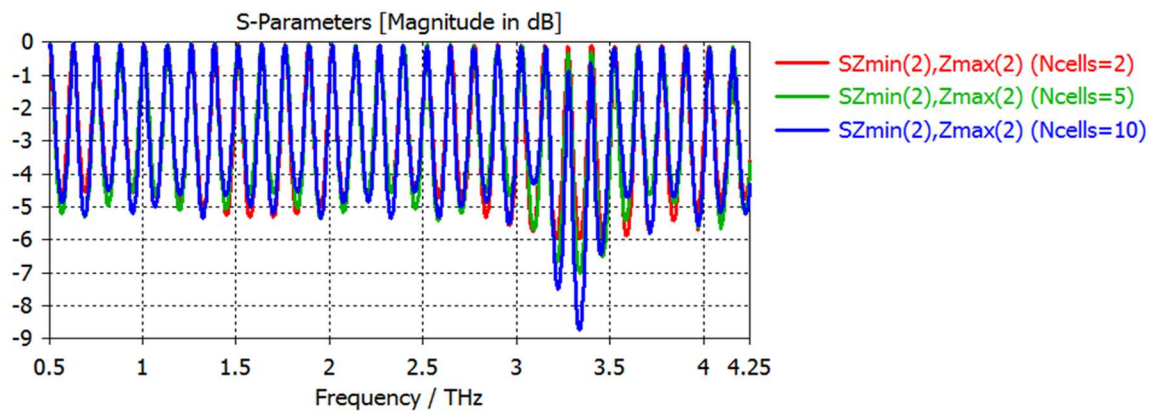

Figure A1. *Preliminary simulations of the transmission of the uncoated SCR (THz) considering a HR-Si substrate in the THz regime for different number of unit cells.*

Figure A1 presents the results of the simulations in the THz regime. On one hand, the SCR (THz) with only two unit cells did not present any remarkable resonances in the whole spectrum simulated. On the other hand, the simulated five unit cells started to show a resonance between 3.0 and 3.5 THz. Moreover, the structure with ten unit cells showed a sharper dip in the same region as the previous case. Thus, a resonance was clearly appearing at 3.3 THz, which corresponds to the resonances experimentally proven in chapter 3.3. The oscillation appeared in Figure A1 corresponds to Fabry-Perot resonances (light bounce back and forth in the Si substrate). This can be eliminated including a time window function similar to the experimental measurements' procedure. However, it is important to continue this study and perform more simulations considering ZnO coated structures to compare with the experimental measurements presented in this work.

Electron beam effect of ZnO coated structures

During the structural characterization of ZnO coated structures in the SEM, we observed the formation of cracks in the ZnO layer upon electron beam illumination.
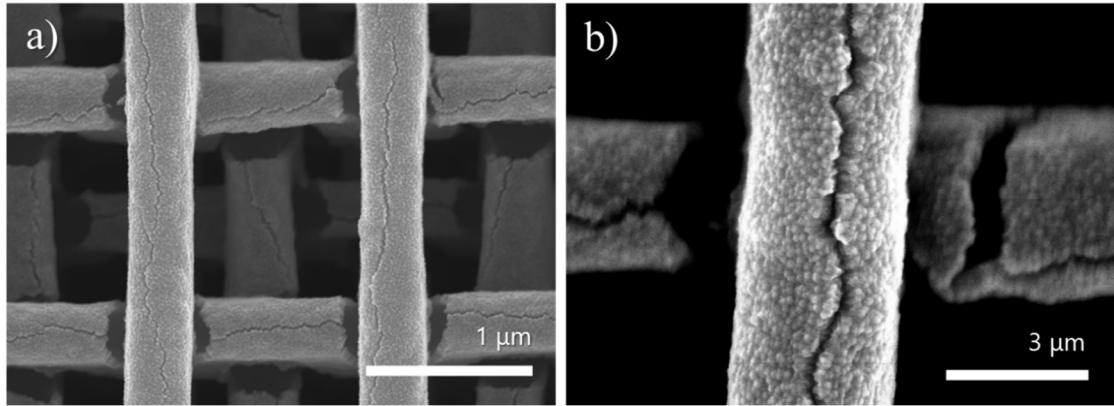
Figure A2. *High-resolution SEM images of the 60 nm ZnO coated WD structures presenting cracks. **a)** Top view and **b)** Close-up.*

As one can observe in Figure A2, cracks were formed along the cylinders in the WD structures. These cracks appeared in the WD when high accelerating voltage (10 kV) and high magnification (x100k) were employed to characterize the structure. It is believed that this phenomenon occurred when the electron beam was tightly focused on the structure, which affected the polymer inside the ZnO coating, causing the polymer to expand and break the thin ZnO layer surrounding it (possible due to volatile species in the polymer). In addition, it is known that ZnO has piezoelectric properties, which could be also the origin of this phenomenon. In all cases, the structural characterization carried out in the thesis was performed with low accelerating voltages to avoid this effect.

Fabrication and testing of mechanical metamaterials with direct laser writing

During the main work, I participated in a side project focused on the fabrication and testing of a mechanical metamaterial, demonstrating the capabilities of the equipment employed and the guide described in this thesis. In this chapter, I present a brief description of the project, which will result in a future publication (in preparation).

Design optimization and structure characterization

The 3D mechanical metamaterial studied is based on the Kelvin Cell geometry, or tetrakaidecahedron, which consists of six flat quadrilateral and eight hexagonal faces (see Figure A3). The overall 3D structure is known as Kelvin Foam (KF).

First, the structure was optimized and fabricated using the IP-S photoresist and the 25x magnification objective (parameters shown in Table A1). While changing some fabrication parameters, it was observed that the density of the structure could be modified using the same modelled design. Thus, in order to perform a complete study, a grid of Kelvin Foam structures was modelled with the slicing changing in every row and the contour distance in every column (see Figure A3). Both parameters were changed in steps of 0.2 µm from 1 µm to 0.2 µm.

Table A1. Optimized fabrication parameters for the KF structure (example shown in Figure A3).

Parameter	Values
Slice (µm)	1 – 0.2
Fill mode	Solid
Hatching distance (µm)	0.3
Contour count	5
Contour distance (µm)	1 - 0.2
Base slice count	10
Hatching angle	120
Hatching angle offset	60
Scan mode	Galvo
Z-axis	Piezo
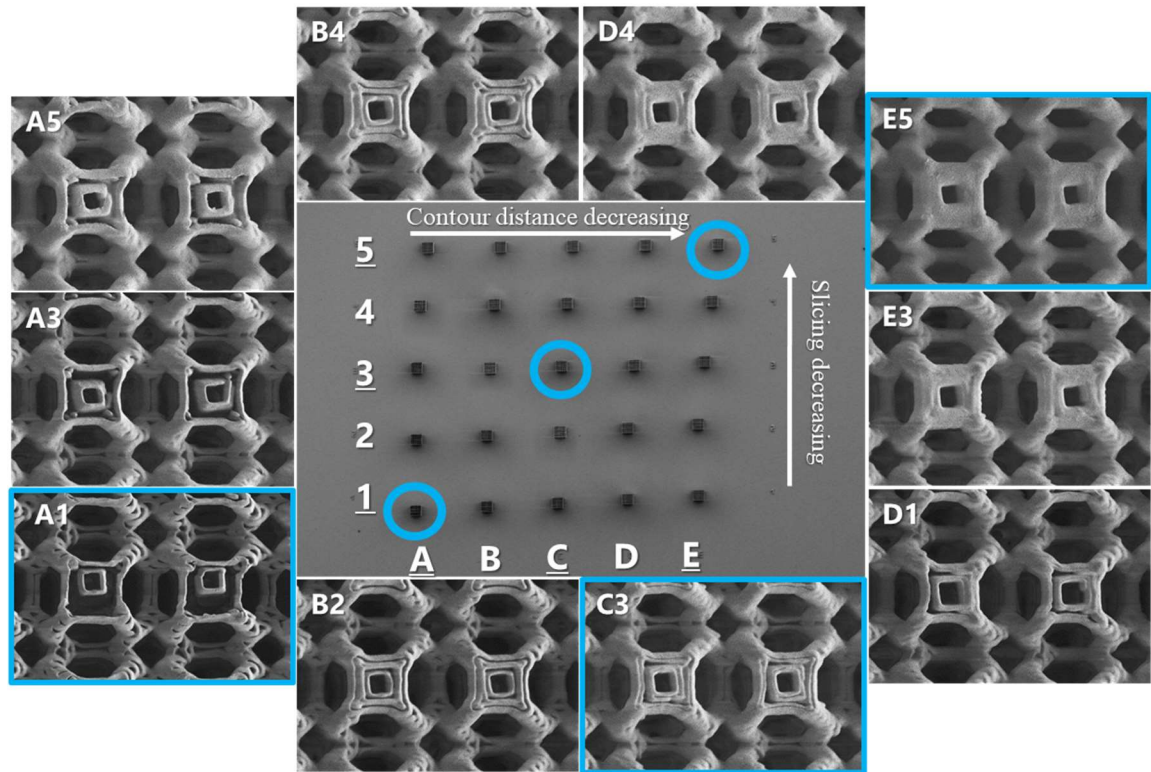
Figure A3. *SEM structural characterization of the KF structures grid fabricated with the optimized parameters presented in Table A1. Top-view images are shown for different illustrative examples. Structures chosen for the posterior study are marked in blue.*

Figure A3 demonstrates how the features and the density of the same modelled design change with different fabrication parameters, being the A1 structure the less dense with a spring-like shape, and the E5 structure the densest with solid features. The structures chosen for the micromechanics study were A1, C3, and E5, which are the ones in the diagonal of the grid. Thus, the same structure with different densities could be compared from a mechanical point of view.

From here, KF structures of A1, C3 and E5, were fabricated. Similar to the 3D metamaterials studied in this thesis, the KFs were coated with ZnO. Thus, five substrates were prepared with the three types of KF in order to coat four with ZnO of different thicknesses (20 nm, 40 nm, 80 nm, 160 nm) and one without coating for reference. In such manner, the study will cover the mechanical properties of a KF structure with different densities and ZnO coating thickness. Importantly, a base and cap were modelled for the KF metamaterials in order to raise the mechanical stability of the structures and compress homogeneously during the micromechanical experiments.
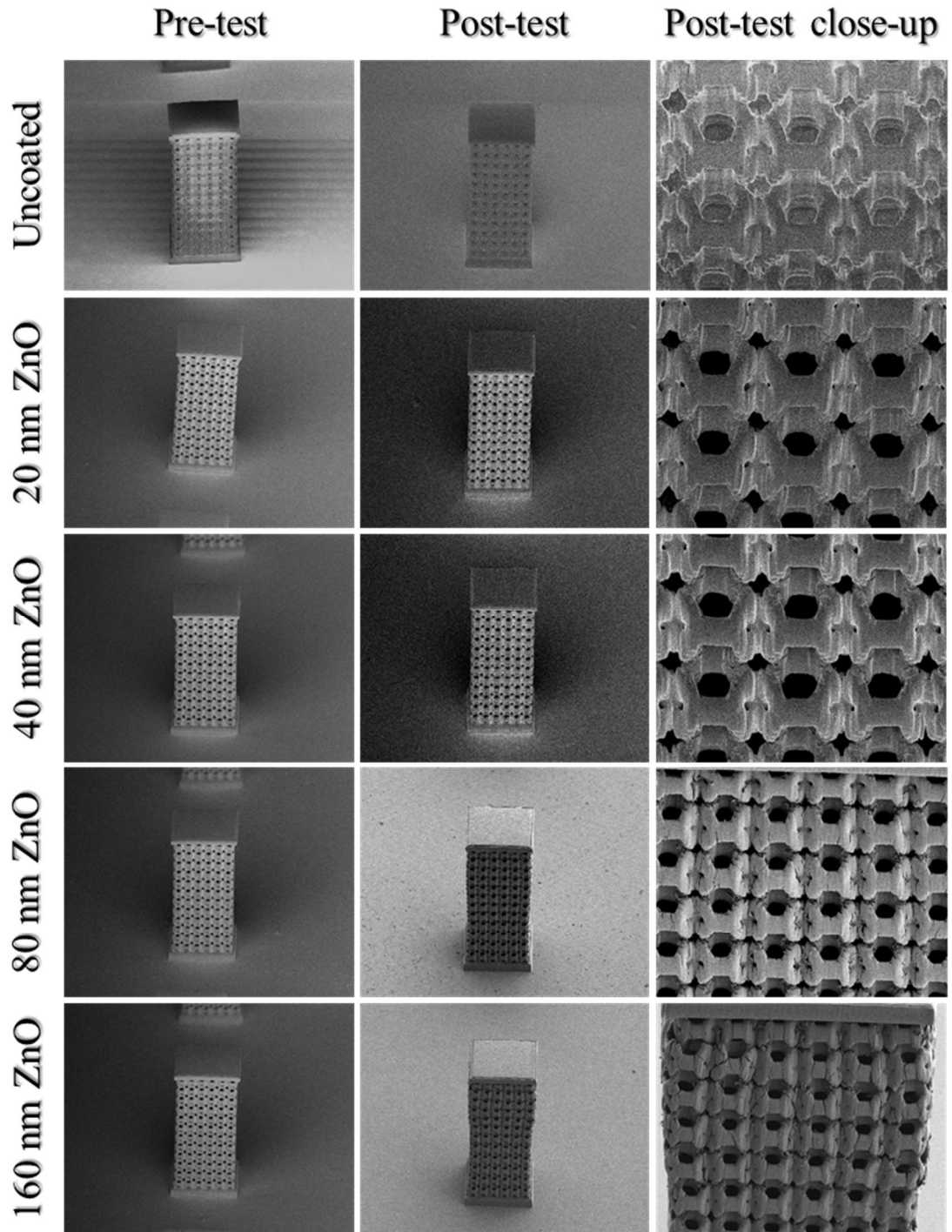
Mechanical testing: Nanocompressions

In this chapter, I acknowledge Dr. Alexander Groetsch for the performance and analysis of the experimental nanocompression measurements.

The mechanical testing was based on the compression of the KF structures with a flat punch. For each type of structure and coating, three different displacement and strain rates were applied: 0.16 μm/s and $1 \cdot 10^{-3}$ s^{-1}, 1.6 μm/s and $1 \cdot 10^{-2}$ s^{-1}, 16 μm/s and $1 \cdot 10^{-1}$ s^{-1}. Here, I only present the quasi-static measurements (see Figure A4), as the other experimental results are still being processed and analysed.
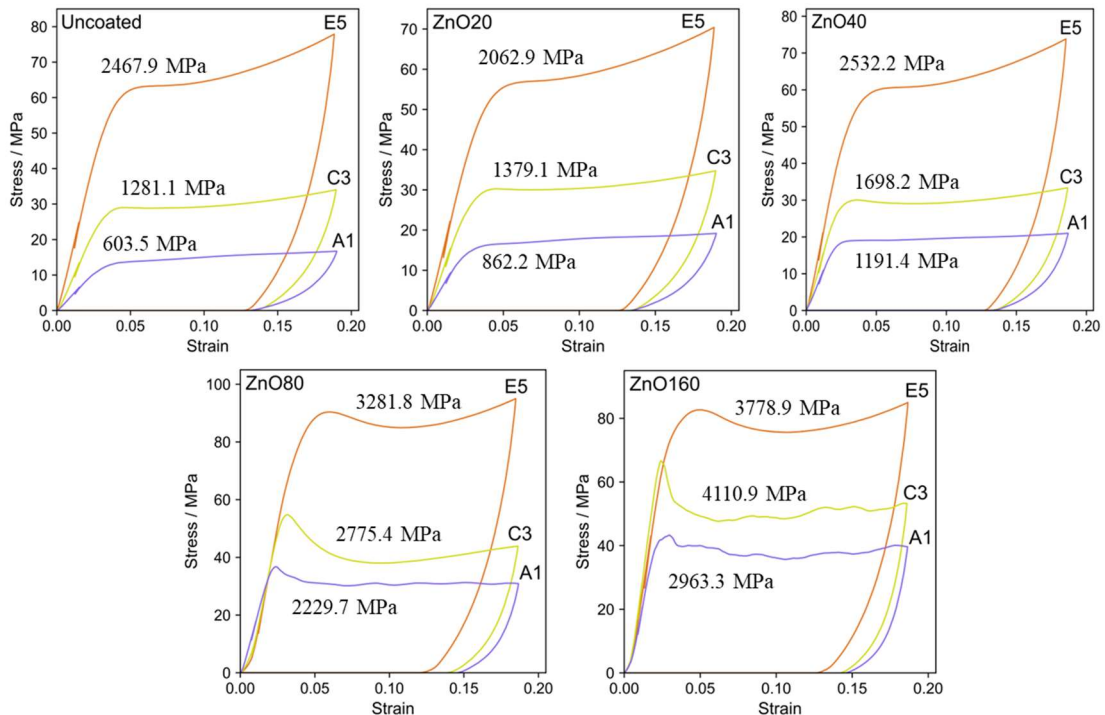
Figure A4. *Stress vs Strain quasi-static curves of the uncoated and ZnO coated (20 nm, 40 nm, 80 nm, and 160 nm) KF structures. Young's modulus (MPa) calculated for each kind of structure and coating is shown.*

As it can be observed, A1 is the weakest structure in all cases, which was expected due to the low density and its spring-like features. On the contrary, E5 is the strongest structure in all cases due to the denser features. The uncoated, 20 nm and 40 nm samples acted as conventional structures with an increase of the Young's modulus as the coating gets thicker. Although, the E5 structure with the 20 nm ZnO coating decreased respect to the uncoated one. In the case of 80 nm and 160 nm, we started to see oscillations for A1 and C3 along the plastic region. It is believed that these oscillations corresponded to the collapse of layers in the structure, thus, the next step was to characterize the compressed structures in the SEM.

Figure A5. *Pre- and Post- micromechanical test SEM characterization of A1 KF structures uncoated and with different ZnO thickness coatings (20 nm, 40 nm, 80 nm, and 160 nm).*

Figure A5 presents the pre- and post- compression SEM characterization of A1 KF structures. On one hand, it can be seen that the structure maintains its shape and features for the uncoated, 20 nm and 40 nm samples, where the height was reduced only by 7 % approximately, while the width was reduced by 4 % approximately. On the other hand, 80 nm and 160 nm samples presented important cracks in the structure, which corresponds to the oscillations observed in Figure A4. In both cases, the height was reduced by 10 % approximately and the width was increased by 5 % approximately. It is noticeable how the quality of the SEM images increases as the thickness of the ZnO coating increases, which corresponds to a decrease of the charging effects in the material. For the C3 and E5 structures, the post- compression SEM characterization presented the same results as the A1 structure, except the E5 with the thicker coatings, which showed less cracks. Note that the scale bar in the images is not shown due to confidentiality reasons.

The KF 3D metamaterials presented extreme robustness and flexibility that such brittle materials (as bulk ZnO) don't have normally. This shows great potential for the nanofabrication of biomimetic tissues due to the ease of choosing different mechanical properties by modifying the fabrication parameters, which allows us to cover a wide range of natural biomaterials.